Corticothalamic Neurons in Motor Cortex Have a Permissive Role in Motor Execution

Lina Marcela Carmona[1], Lin T. Tun[1], An Kim[1], Rani Shiao[2], Michael D. Kissner[3], Vilas Menon[4], Rui M. Costa[1,5]

[1] Department of Neuroscience, Zuckerman Mind Brain Behavior Institute, Columbia University, New York, NY, USA
[2] Laboratory of Molecular Genetics, The Rockefeller University, New York, NY, USA
[3] Columbia Stem Cell Initiative, Columbia University Irving Medical Center, New York, NY, USA
[4] Center for Translational & Computational Neuroimmunology, Department of Neurology, Columbia University Irving Medical Center, New York, NY, USA.
[5] Allen Institute, Seattle, WA, USA.

ABSTRACT

The primary motor cortex (M1) is a central hub for motor learning and execution, as it receives input from and broadcasts to a multitude of other motor regions. It has become increasingly clear that M1 is heterogeneous in terms of cell types, many of which exhibit varying relationships to movement during learning and execution. Previous studies have mainly used a single candidate approach to identify cell types contributing to motor learning and execution. Here, we employed an unbiased screen to tag active neurons at different stages of performance of a motor task. We characterized the relative cell type composition among the active neurons at different stages of motor training and identified varying patterns across training. One cell type consistently showed enrichment as training and execution progressed: corticothalamic neurons ($M1^{CT}$). Anatomical characterization of $M1^{CT}$ neurons revealed an extensive projection pattern to thalamic nuclei with marked topographical organization. Using two-photon calcium imaging, we found that $M1^{CT}$ neuron activity is largely suppressed during movement. $M1^{CT}$ neurons display a negative correlation with movement that scales with movement vigor and augments with training. Closed-loop optogenetic manipulation of $M1^{CT}$ activity revealed that their activity rapidly affects movement execution, even after movement is initiated. Taken together, these results identify and reveal a critical permissive role of corticothalamic neurons in movement execution.

INTRODUCTION

The ability to learn and execute new movements is critical for survival. Precise execution of movements is often acquired via repetition and refinement, a process that depends on activity coordinated throughout the brain and spinal cord[1,2]. Within these circuits, the primary motor cortex (M1) projects directly to the spinal cord, but also to other motor areas in basal ganglia, thalamus and brainstem, affording it unique control over motor action[3,4]. M1 is engaged during motor learning as well as during the execution of voluntary movements in rodents, non-human primates, and humans[5-12]. Changes in the formation, turnover, and spatial distribution of spines[13-17], the restructuring of dendritic arbors[18-21], as well as shifts in the patterns of electrical activity in M1 all affirm the critical role of M1 in learning and performance of various motor tasks[11,15,22-27].

However, M1 cells are transcriptionally and functionally heterogeneous[28-30], and it is clear that different cell types exhibit varying relationships to movement during learning and/or execution. Some recent studies have tried to isolate the role of different M1 cell types in movement or learning by using known cell type markers or projection patterns[22,23,31]. We reasoned that a more unbiased and comprehensive screen of which cell types are engaged during movement, at different stages of training and proficiency, could complement the candidate approach taken to date. We designed an experimental approach leveraging a calcium-dependent photoswitchable indicator in combination with single-cell RNA sequencing to determine which M1 cell types are differentially enriched at different stages of motor training and proficiency. This approach identified several neuron types within M1 with differential activity early versus late in training and led us to uncover that a particular cell type – the M1 corticothalamic neurons – have an unexpected but critical role in movement.

RESULTS

$M1^{CT}$ neurons are enriched at late stages of training

We utilized an M1-dependent head-fixed motor task[32] to screen for cell type engagement at different stages of training. The task consists of forelimb-driven pulls of a small rotary wheel wherein mice had to cross an IR beam at the apex of the wheel and make contact with the rungs to commence a trial (Figure 1A). Mice were rewarded when pulls executed within 200ms of trial start reached a velocity threshold. Within two weeks, mice showed an increase in the number of successful trials, as demonstrated by significantly increased percent success over time ($p=0.0104$, one-way ANOVA, time) (Figure 1B), as well as increased velocity of trials, as indicated by an increase in the maximum velocity reached during all trials in each training session ($p=0.0182$, one-way ANOVA, time) (Figure 1C,D). For subsequent experiments, we chose day 4 and day 12 as our early and late training time points, respectively ($p=0.0336$, day 4 v. day 12, one-way ANOVA).

We next optimized a system to label the neurons that were active at different stages of execution of this task. To this end, we utilized CaMPARI, a photoswitchable indicator that fluoresces green at baseline but converts to red upon coincident exposure to calcium and 405 nm light[33] (Figure 1E). Although there are numerous systems now available to label active neurons[34-37], CaMPARI was particularly well suited for our approach given its high fidelity reporting of activity relative to Immediate Early Gene (IEG) systems, and its short window of labeling (on the order of seconds) compared to hours for other systems. We performed stereotactic injections of an adeno-associated virus (AAV) expressing CaMPARI under the neuron-specific human synapsin promoter into the caudal forelimb region (CFA)[38,39] of M1. We compared cell type engagement at

different training stages: 1) early stages of training (day 4), 2) late stages of training (day 12), and 3) no training, in which the wheel was covered but the mouse was otherwise exposed to the same environment. On the day of the respective time point, light was delivered through a cranial window in pulses of 5s as mice performed or were exposed to the task to photoswitch CaMPARI and label the active neurons (Extended Data Figure 1). M1 was then rapidly dissociated and neurons with photoswitched red CaMPARI fluorescence were enriched using fluorescence activated cell sorting (FACS). This ensured that only "active neurons" were subsequently processed using single-cell RNA sequencing. All timepoints were repeated a minimum of four times to account for behavioral variability, and we achieved a median unique molecular identifier (UMI) and gene count of 7971.5 and 3503, respectively, over all runs (Supplementary Table 1).

Unbiased clustering of our aggregate data yielded the expected subdivisions based on cortical layer marker genes. Mapping to a high resolution M1 cell type atlas[28,29] further demonstrated the cell type heterogeneity present in our samples, with concordance among our clusters and their mapped annotations (Figure 1F, Extended Data Figure 2A,B). Comparison of the cell types present at each timepoint did not reveal a binary presence or absence of a particular type (Extended Data Figure 2C). Rather, enrichment analysis demonstrated a diversity of cell type engagement patterns across timepoints (Figure 1G,H). It should be noted that we did not capture as many inhibitory neurons across timepoints, and therefore, conducted our enrichment analysis independently for excitatory and inhibitory neurons. To control for labeling dependency on light penetration and differential baseline activity of neuronal types, we used internal comparisons by calculating enrichment relative to the control condition. Overall, compared to the control condition that did not receive any training, the most enrichment occurred across clusters in late condition with one and two subtypes enriched in excitatory and inhibitory neurons, respectively. In comparison, only one inhibitory and one excitatory subtype were enriched in the early condition relative to the control condition. When comparing the two task time points (early and late training stages), we observed enrichment of four subtypes, two excitatory and two inhibitory, at late stages of training, and enrichment of three inhibitory subtypes at early stages. Only one subtype showed significant enrichment relative to the control ($p=0.009975$, Bonferroni-adjusted) and between the two training stages ($p=0.000921$, Bonferroni-adjusted): the corticothalamic neurons ($M1^{CT}$) marked by FoxP2 expression (excitatory cluster 9, e9). Given this enrichment at late stages of learning, as well as the known role of thalamus in motor learning and execution[40-42], we further investigated the role of these neurons during motor execution.

Topographical organization and projection pattern of $M1^{CT}$ neurons

Given that this population of neurons and their connectivity have been relatively understudied, we started by investigating the extent and architecture of the connection between this subset of motor cortex neurons and specific subregions of thalamus. We labeled FoxP2 expressing neurons by injecting an AAV expressing a Cre-dependent membrane bound green fluorescent protein (GFP) into M1 of FoxP2-cre animals (Figure 2A). We cleared intact brains and amplified the signal with antibody labeling using a modified Adipo-Clear tissue clearing protocol[43]. Whole mount light sheet imaging and the ClearMap image analysis pipeline[44] were used to detect the GFP signal within thalamus and map to a common brain atlas (Extended Data Figure 3A). We observed that $M1^{CT}$ neurons target numerous thalamic nuclei, in agreement with other studies[4,45,46] (Figure 2B-D). These included primary targets such as those of the motor thalamus, like the ventral anterio-lateral (VAL) and posterolateral nuclei (VPL), as well as the posterior complex (PO).

Neurons that target different regions of thalamus may be biased in their distribution in motor cortex, as well as the intensity of their projections to their thalamic targets. To examine the logic of this connectivity matrix, we divided the majority of the observed thalamic projection density into

three broad groups: medial, ventral, and lateral. We retrogradely labeled thalamus-projecting M1 neurons by injecting Fluoro-Gold into each of these groups (Figure 2E). We used BrainJ[47], an image analysis pipeline for machine learning based segmentation, to identify fluorogold-labeled neurons across cortex. We then mapped the position of these neurons to a common atlas[47] (Extended Data Figure 3B,C). The majority of neurons were found in layer VI of cortex for all tested thalamic regions, and the largest number of cortical neurons were detected in labeling from the ventral region (Figure 2F; $p=0.0020$, lateral v. ventral; $p=0.0400$ ventral v. medial; two-way ANOVA). This held true both within the caudal forelimb area (CFA) of M1 (Extended Data Figure 4A, Extended Data Figure 5) and in primary somatosensory cortex (Extended Data Figure 4B-D), but not for secondary motor cortex or supplementary somatosensory cortex (Extended Data Figure 4 E-J), further demonstrating the specificity in targeting of thalamus by these sensorimotor cortical areas.

Of all M1 layer VI neurons, those that targeted ventral thalamus were the most broadly distributed throughout cortex (Figure 2G). Conversely, the lateral and the medial thalamus-targeting neurons were enriched along the anterior/posterior axis of M1 with the medial group enriched in the anterior portion and the lateral group enriched in the posterior portion (Figure 2H,I; $p<0.001$ and $p=0.0173$ for medial v. lateral in anterior and posterior M1, respectively, two-way ANOVA.). A similar distribution was observed for layer V (Extended Data Figure 4). Together, these data demonstrate that there are broad and topographically organized M1 projections to thalamus, and place $M1^{CT}$ neurons in a critical position to broadcast motor information to thalamic nuclei.

$M1^{CT}$ neurons decrease activity during movement

The contribution of the corticothalamic M1 output pathway to motor execution is poorly understood as compared to the thalamocortical pathway[48,49]. Thus, we characterized the activity of $M1^{CT}$ neurons at different stages of training in our wheel pulling task. We performed stereotactic injections to deliver AAV expressing Cre-dependent GCaMP7f to CFA in M1 of FoxP2-cre mice (Extended Data Figure 6A). To image activity of these deep cortical neurons without incurring significant damage to M1, we followed an approach previously implemented to image corticospinal neurons in M1[23,27]. We used two-photon (2p) imaging to record calcium dynamics in the dendrites of FoxP2+ $M1^{CT}$ neurons through a cranial window at a depth of at least 300 μm below pia. To extract the calcium signal, we used constrained nonnegative matrix factorization (CNMF)[50], and we excluded any highly correlated units ($\rho>0.8$) to avoid overrepresentation from branches of the same neurons[23,51] (Extended Data Figure 6A).

We analyzed $M1^{CT}$ activity during movement by aligning to trial start during successful or unsuccessful trials across all training sessions. Surprisingly, we observed that activity of $M1^{CT}$ decreased during wheel movement (Figure 3A,B; Extended Data Figure 6B). To examine whether this was a general feature of these neurons, we calculated the cross-correlation of the activity ($\Delta F/F$) to the wheel velocity as measured by the rotary encoder. This further demonstrated a negative relationship between activity and wheel movement throughout the session, with the suppression in neuronal activity slightly preceding peaks in wheel velocity (Figure 3C). Given this striking signature in M1 where other populations exhibit positive correlations with movement[23,27,31], we examined whether the suppression in $M1^{CT}$ neurons was observed for the majority of $M1^{CT}$ neurons. For this, we examined activity during all wheel pulls of all sessions and found a similar decrease in activity during movement as in trials (Extended Data Figure 6C). ROC based classification revealed that most neurons show a decrease in neuronal activity during wheel pulls (69%, $M1^{CT\text{-}down}$) relative to a window of low movement prior to the pull compared to those showing no modulation (15%, $M1^{CT\text{-}none}$) or increased activity (16%, $M1^{CT\text{-}up}$) during wheel movement (Figure 3D-G).

Furthermore, for the neurons that decreased in activity, the magnitude of the decrease changed depending on the velocity of the movement. When we grouped pulls of varying velocity into bins (2-6 cm/s, 6-10 cm/s, 10-14 cm/s, >14 cm/s), we observed larger decreases in activity for higher speeds (Figure 3H-J; for min of ΔF, $p<0.0001$, 2 to 6 v. 6 to 10 and 6 to 10 v 10 to 14; $p=0.0553$, 10 to 14 v 14 and up, two-way ANOVA), but no change in the timing of maximal suppression (Extended Data Figure 7A). This scaling was also reflected in the magnitude of cross-correlation of the velocity bin groups (Extended Data Figure 7B). The graded response appeared specific to $M1^{CT\text{-}down}$ neurons as no relationship in activity magnitude and wheel velocity was observed in $M1^{CT\text{-}up}$ or $M1^{CT\text{-}none}$ neurons (Extended Data Figure 7C,D).

Interestingly, we observed an increase in the modulation range of neurons around movement from early to late learning (Δ F/F max – min), consistent with the enrichment in CaMPARI labeling with training (Extended Data Figure 8A). We therefore examined if the correlation also changed over the span of training sessions. We observed a significantly larger anti-correlation during late training sessions compared to early (Figure 3L,M) in $M1^{CT\text{-}down}$ neurons. No difference was observed in the relative proportions of the population (Extended Data Figure 8B). Given that as mice progressed through the task they tended to perform higher velocity pulls (Figure 1C, Extended Data Figure 8C), we examined the anti-correlation in early and late session neurons for pulls of matched velocities. Even in subsets of pulls with a similar distribution of peak velocities (Extended Data Figure 8C), we found a consistent increase in the magnitude of the anti-correlation to wheel movement at late training (Figure 3M, Extended Data Figure 8D; for early v. late, $p<0.001$, 2 to 6, 6 to 10, and 14 and up; $p=0.005$, 10 to 14, one-way ANOVA). These results indicate that $M1^{CT}$ neurons are predominantly suppressed during movement and show a negative correlation with movement that is modulated by speed and increases with training.

$M1^{CT}$ suppression is permissive for motor execution

We hypothesized that the decrease in $M1^{CT}$ neuronal activity was critical for movement execution during late stages of training, and that disrupting this decrease in activity would affect movement speed. To test this, we performed a closed-loop optogenetic manipulation on a subset of trials at the late training stage. Given that these neurons decrease in activity during wheel pulls, we chose to activate them during this time window to disrupt this expected decrease. To achieve this, we performed stereotactic injections of an AAV into CFA of M1 to express Cre-dependent channelrhodopsin (hChR2) or a fluorescent protein in Foxp2-cre animals, generating our opsin and control groups respectively. We then trained both groups of animals to the late training stage and delivered 400 ms of pulsed light at the onset of one third of trials (20 hz; 10 ms pulse width, Figure 4A). Overall, this manipulation decreased the number of successful trials performed with the light on in opsin expressing animals but not in control animals (Figure 4B,C; for percent of successful trials, $p=0.0119$, two-tailed unpaired t-test; for percent success, $p=0.7031$ and $p=0.0014$ for control and hChR2, respectively, two-way ANOVA). Importantly, when we compared the way in which trials were executed with or without light, we found a drastic decrease in wheel velocity ($p=0.8713$ and $p=0.0003$ for control and hChR2, respectively, two-way ANOVA) as well as pull distance ($p=0.9511$ and $p=0.0027$ for control and hChR2, respectively, two-way ANOVA) in light-on trials of opsin animals (Figure 4D-F, Extended Data Figure 9). Furthermore, this decrease in velocity was rapid, and observed in less than 200ms ($p<0.0001$ and $p>0.9999$ for opsin and control, respectively; two-way ANOVA for first 200ms after light on, time x condition).

While these results showed that disruption of the activity of these neurons impaired proficient execution of task-related movements, it did not indicate whether modulation of $M1^{CT}$ neuronal activity is still important after movement is already ongoing and peak velocity has been achieved.

We, therefore, performed a closed loop manipulation on a new cohort of animals but delivered light around the time of maximum trial velocity, rather than trial initiation (Figure 4G, light delivered 110 ms after trial start). As expected, there was no change in the percent of successful trials or maximum velocity of trials as mice had already reached peak velocity before the light was turned on (Figure 4I, Extended Data Figure 10B,C). However, we observed that even after movement started, there was a rapid and drastic decrease in movement speed following inhibition (Figure 4H,J, Extended Data Figure 10D-I). Finally, we tested whether stimulating these neurons before movement initiation (i.e. to avoid the decrease in activity even before movement starts) would affect task execution. We performed an open loop optogenetic manipulation, randomly delivering light for 1.2 s over 1/10th of the behavior session (Figure 4K). When we examined wheel pulls similar to those executed during trials but where light was delivered before trial initiation (50-75ms before the peak of the pull), we observed a decrease in both velocity ($p=0.1558$ and $p=0.0016$ for control and hChR2, respectively, two-way ANOVA) and wheel pull distance (Figure 4L-N, Extended Data Figure 10J; $p=0.0708$ and $p=0.0011$ for control and hChR2, respectively, two-way ANOVA). Together, these manipulations highlight that ontogenetically activating M1^{CT} neurons at precise movement times when their activity decreases rapidly impairs movement execution regardless of the phase of movement, and strongly suggest that the decrease in activity of M1^{CT} neurons is permissive for movement.

DISCUSSION

Our studies identified M1^{CT} neurons as a key permissive population for motor execution. We first identified this population using an activity-based, single-cell RNA-seq based screen of M1 during the progression of a motor task. Mapping of M1^{CT} neurons showed broad targeting of thalamus and marked topographical organization. Experiments characterizing the dynamics of M1^{CT} neurons showed that most of these neurons have a marked suppression during movement. Accordingly, closed-loop experiments revealed that optogenetic activation of these neurons at different moments of movement execution rapidly and substantially impaired execution, suggesting that the decrease in activity is permissive for movement execution. This is one of the first thorough examinations of the contribution of this M1 output pathway to movement.

Our activity-based screen fills a niche in exploring cell type specific contributions to short time scale behaviors. Identifying the cell types with patterns of engagement during a particular behavior complements hypothesis-driven investigation of the role of particular cell types. This can then be followed by confirmatory techniques for neuronal activity recording, such as calcium imaging, which allow for in-depth characterization of particular activity patterns. Whereas we chose to focus on a cell type that differed in enrichment with training, it may also be informative to examine cell types that constitute the largest part of the active ensemble at a given point. In our experiments, we observed greater numbers of several IT subsets at the time points assessed. This could imply that these neurons are generally active for cortical processing regardless of the specific ongoing behavior. Although our screen is not comprehensive, it still allowed us to compare differential cell type engagement during training. As new tools emerge, they may allow for similar but more quantitative approaches for identifying active cell types in the future.

There has been a long-standing interest in defining the role of the primary motor cortex and its relationship to movement. For example, most M1 corticospinal neurons, which project directly to the spinal cord and are hence relatively proximal to skeletal muscle, have been shown to have movement correlated activity[27]. Similarly, intratelencephalic neurons projecting within cortex show increased activity during movement[31]. In contrast, our imaging of M1^{CT} neurons shows that the majority of this population reduces activity at the time of movement. This dichotomy in activity

could be related to the projection patterns of these neurons. Some corticopontine neurons, which also project to thalamus, also show reduced activity during movement[31]. Furthermore, it would be interesting to determine if some corticospinal neurons that show a decrease in activity also project to thalamus[23,27]. Therefore, examining specific cell types with more granularity could help explain the heterogeneity observed in the activity of primary motor cortex in motor tasks.

Our closed-loop optogenetic experiments suggest that activation of $M1^{CT}$ neurons at a time when they should be suppressed rapidly and profoundly impairs movement execution. This permissive activity signature of $M1^{CT}$ neurons could prioritize other signals originating from M1, such as corticospinal and IT neurons, or inputs coming into thalamus from regions other than motor cortex, thus effectively switching information processing channels in the cortico-thalamocortical loop. Furthermore, we observed a topographic patterning among the CT neurons in M1. In conjunction with the somatotopy present in M1, this could suggest that regions contributing to the control of different body parts may differentially target these thalamic regions. For example, the forelimb representations in M1 are divided between rostral and caudal forelimb area (RFA and CFA), with the latter showing significantly more $M1^{CT}$ neurons that project to the ventral and lateral regions than the medial region (Extended Data Figure 5). Examining the activity of cortex and thalamus within these subregions may elucidate whether these projection patterns correspond to functional specificity in the cortico-thalamic connections.

ACKNOWLEDGEMENTS

We are grateful to C. L. Warriner for sharing a prior iteration of the wheel turning task; H. Rodrigues, for assistance designing and constructing behavioral equipment; I. Shieren, G. Martins, and M. Correia for technical assistance; A. Nelson for discussion and feedback on the manuscript; L. Hammond, D. Peterka, and H. Ibarra Avila for assistance with various types of imaging and imaging data analysis; and T.M. Jessell for invaluable enthusiasm and support when this project was devised. Imaging was performed with support from the Zuckerman Institute's Cellular Imaging platform, and the National Institute of Health (NIH 1S10OD023587-01). L.M.C. was a Hellen Hay Whitney Foundation Fellow and is currently supported by a NIH Pathway to Independence Award (1K99NS127857-01). R.M.C. was funded by grants from the NIH (5U19NS104649) and the Simons-Emory International Consortium on Motor Control.

AUTHOR CONTRIBUTIONS

L.MC., R.M.C., and V.M. designed experiments and interpreted data; L.M.C. performed experiments and analyzed data; L.T. collected and analyzed anatomical data; A.K. assisted in experimental optimization; R.S. assisted with tissue clearing; and M.D.K performed all flow cytometry; and L.M.C and R.M.C. wrote the manuscript.

MATERIALS AND METHODS

Mice

All experiments and procedures were performed according to National Institutes of Health (NIH) guidelines and approved by the Institutional Animal Care and Use Committee of Columbia University. Adult mice of both sexes, aged 2–6 months, were used for all experiments, except for RNA sequencing which only used males aged 3 months. The strains used were: C57BL6/J (Jackson Laboratories, 000664), FoxP2-Cre (Jackson Laboratories, 030541). Only mice used for RNA sequencing experiments were individually housed. All mice were kept under a 12-h light-dark cycle. All mice except those used for calcium imaging experiments were kept under reverse light cycle conditions.

Viral Vectors

For CaMPARI based experiments, AAV1-hSyn-CaMPARI (Addgene 100832-AAV1) was used. Projection mapping was performed with the membrane bound GFP expressed from AAV8-hSyn-JAWS-KGC-GFP-ER2 (Addgene 65014-AAV8). Calcium imaging experiments were performed with AAV1-Syn-FLEX-jGCaMP7f (Addgene 104492-AAV1). Optogenetic experiments used AAV1-Ef1a-DIO-EYFP (Addgene 27056-AAV1) and AAV1-EF1a-DIO-hChR2 (H134R)-EYFP (Addgene 20298-AAV1) for control and opsin animals respectively.

Stereotactic surgery

Animals were anesthetized using isofluorane, and analgesia was delivered subcutaneously in the form of either carprofen (5 mg/kg) or burprenorphine SR (0.5-1 mg/kg) as well as bupivacaine (2 mg/kg). For all viral vectors delivered to M1, injections were centered in the caudal forelimb area (CFA) using the following coordinates: 1.5 mm lateral to the midline, 0.25 mm rostral to bregma. A total of 5 injections were made in this region to cover a large portion of CFA in the contralateral (left) hemisphere. Specific sites were adjusted to avoid blood vessels. A Nanoject III Programmable Nanoliter Injector (Drummond Scientific) was used at a rate of 1 nl/s.

For CaMPARI experiments, a total of 1 uL of virus was delivered (200 uL at each of the five injection sites) at a range extending to 800 um below the pial surface (25 uL every 100 um). For projection mapping, a total of 500 uL of viral vector was injected (100 nL per injection site) from 900-500um below the pial surface (20 nL at every 100 um). For calcium imaging, a total of 375 uL of viral vector was injected (75 nL per injection site) from 950-650 um below the pial surface (25 nL at every 100 um). For optogenetic experiments, a total of 500 uL of viral vector was injected (100 nL per injection site) from 850-650um below the pial surface (20 nL at every 100 um). To prevent backflow, we waited 3-5 minutes before the initial injection and 5-10 minutes after each injection. For animals used in behavioral experiments, a headplate was attached to the skull with Metabond (Parkell) post injection.

For retrograde labeling from thalamus, we used the following coordinates, for the ventral region: 1.3 mm lateral from the midline, 1.22 mm caudal to bregma, and 3.5 mm below the pial surface; for the lateral region: 1.25 mm lateral from the midline, 2.18 mm caudal to bregma, and 3.25 mm below the pial surface; for the medial region: 0.1 mm lateral from the midline, 1.46 mm caudal to bregma, and 4.2 mm below the pial surface. A total of 10 nL of 4% FluoroGold (Fluorochrome) was injected. FluoroGold was freshly diluted the day of injection from a 10% stock solution. To prevent backflow, we waited 2 minutes before each injection and 10 minutes after each injection.

Cranial window implantation

For animals requiring a cranial window, surgery was performed as described above with the following modification. Animals were anesthetized using isofluorane, and analgesia was delivered subcutaneously in the form of burprenorphine SR (0.5-1 mg/kg) and bupivacaine (2 mg/kg). Dexamethasone (2 mg/kg) was also delivered as an anti-inflammatory agent. A larger craniotomy

was made (2.5 mm in diameter) for a custom cranial window made of a glass plug (2.5 mm diameter) attached to a larger glass base (3.5 mm in diameter) with optical cement (Norland Optical Adhesive 61). After viral injection, the cranial window was implanted to gently press on the brain at the site of the craniotomy and secured with Metabond (Parkell). Headplate implantation followed cranial window implantations.

Behavior

Several noise attenuating behavioral chambers equipped with IR light were assembled with custom components to train several animals in parallel. Mice were placed in flat bottom, opaque tube, and head fixed using a custom metal headplate by screwing in place to adjustable head posts. The small rotary wheel was directly below the right forelimb of the animal when in the holder. A small partition prevented animals from utilizing their left forelimb to pull the wheel. A small screw was also provided for left forelimb placement. Mice were habituated to head fixation and water delivery via the water port for several days before the beginning of training. The water port consisted of a blunt needle positioned in front of the mouse so water was reachable by licking. Water droplets were generated using a solenoid valve and were calibrated before the beginning of training for each experiment. The 60 mm diameter rotary wheel was assembled from two acrylic sides held together by small metal screw rungs. An absolute rotary encoder (US Digital; 10 bit) was placed in the shaft of the wheel to assess wheel movement. Each rung was wired to a capacitance sensor. An IR beam was placed at the apex of the wheel on a custom 3D printed holder allowing for alignment of the beam. Data from all behavioral components was collected using a DAQ (National Instruments) sampling at 2000 Hz. Behavioral sessions were controlled using custom MATLAB code which assessed beam breaks and changes in rung capacitance. If thresholds were met, a trial would commence and wheel displacement was then assessed, smoothed, and converted to velocity. If the threshold velocity was surpassed, a pulse was sent to the solenoid to deliver the water reward. Mice were habituated to the task during three pretraining sessions prior to the beginning of training. During these sessions, mice were exposed to the task but at low trial velocity thresholds for a limited number of trials. Training sessions consisted of 30 minutes daily or a maximal of 100 successful trials. Mice were trained during the dark phase of their reversed light cycle housing schedule.

CaMPARI labeling

Four weeks post injection, mice were head-fixed as in all behavioral experiments and a plastic fiberoptic patch cord (960 um core; 0.63 NA) ending in a metal ferrule (Doric) was placed directly over the cranial window. A multichannel LED driver (Doric) was used with 405nm central wavelength connectorized LED (Doric, ~60 mW). Concurrent with the start of the training session, light delivery was initiated using the Doric Neuroscience Studio software. Light was delivered in square wave pulses of 5s each with 5s of light off between each pulse for a total of 12 minutes.

Generation of single-cell suspensions and FACS

After CaMPARI labeling, mice were returned to their home cage for 15 minutes and then euthanatized by transcardial perfusion with ice-cold choline solution as previously described[52]. M1 was quickly dissected, and single-cell suspensions were generated using the previously described protocol optimized for preserving transcriptional state with the following modifications[52]. The dissected M1 tissue was further triturated with spring scissors. Incubation with papain was conducted using a dialysis membrane (Fisher Scientific, Slide-a-Lyzer MINI Dialysis Device,10k molecular weight cut-off) suspended in a beaker of dissociation solution allowing for constant oxygenation (95% O_2 and 5% CO_2) of the solution without disrupting enzyme integrity within the dialysis membrane. After enzymatic dissociation, the tissue was broken into a single-cell suspension by gently pipetting using wide-bore pipette tips. The sample was cleaned using the

Debris Removal Solution (Miltenyi Biotec) as described by the manufacturer. Cells were suspended in dissociation solution containing 0.04% BSA, Vybrant DyeCycle Ruby for exclusion debris, and RNAase inhibitors. Cell sorting was performed using a FACSAria Cell Sorter (Becton Dickinson) with a 130 um nozzle at 12 PSI using the following laser lines and filters: CaMPARI Green, 488 nm, 530/30 bandpass; CaMPARI Red, 561 nm, 610/20 bandpass; DyeCycle Ruby, 637 nm, 670/30 bandpass. Gates were set using a sample not expressing CaMPARI and a sample not exposed to photoconversion light (Supplementary Figure 1.1B). Any cells with detectable red fluorescence were collected.

Single-cell RNA-seq

Sorted cells were captured and barcoded using 10x Genomics Chromium v3 according to the manufacturer's protocol. Samples were processed and libraries were prepared and sequenced by the JP Sulzberger Columbia Genome Center Single Cell Analysis Core.

Single-cell RNA-seq analysis

Single-cell RNA-seq analysis followed a standard workflow, comprising the following steps:

1) Sequencing read files were aligned to the mm10 genome using 10x Genomics Cellranger v.3.1.0, generating a table of cell barcodes by Unique Molecular Identifier (UMI) counts per gene.
2) Raw counts files were aggregated, and cells with >20% UMIs mapping to mitochondrial genes were removed, as well as cells with <200 UMIs after removing mitochondrial genes, ribosomal protein genes, pseudogenes, and gene models**.**
3) Cells were clustered using the Seurat R package (v.4.0.0), with SCTransform (default parameters) and PCA, followed by integration across batches using the Harmony R package (with 40 PCs). The cell-cell neighbor network was constructed with 30 Harmony dimensions, and the Louvain community detection algorithm was run with resolution = 0.4.
4) Based on expression of marker genes for neurons and glia (Snap25, Slc17a6, Slc17a7, Gad1, Gad2, Mbp, Mog, Fgfr3, Aqp4, Pdgfra, Tmem119, Aif1, Ptprc, and Cldn5), the clusters corresponding to glutamatergic and GABAergic neurons were extracted.
5) Step 3 was re-run on the glutamatergic and GABAergic neurons (separately), with 30 PCs, 20 Harmony dimensions, and resolution = 0.2.
6) Combinatorial marker genes were identified for each cluster using the FindMarkers command in Seurat, run on all pairs of clusters. In parallel, putative layer identities for each cluster were assigned by mapping to Azimuth Mouse Motor Cortex reference.
7) To assess differential proportions among conditions, cell count values were run through the ANCOM-BC R package, with pairwise comparison between control, early, and late conditions. All q-values were then further Bonferroni-corrected.

Projection mapping

Mice were euthanized by intracardial perfusion with 1× PBS followed by 4% paraformaldehyde. Brains were post-fixed in 4% paraformaldehyde overnight at 4 °C. The AdipoClear protocol was performed as previously described[43] with the following modifications. Primary and secondary antibody incubations were conducted at 37 °C and for 6 days per incubation. The following primary antibodies were used at a dilution of 1:2500: chicken GFP antibody (Aves) and rabbit RFP antibody (Rockland). The following secondary antibodies were used at a dilution of 1:2500: donkey anti-rabbit Alexa Fluor 647 (ThermoFisher Scientific) and donkey anti-chicken Alexa Fluor 647 (ThermoFisher Scientific). Samples were imaged with a light-sheet microscope (Ultramicroscope II, LaVision Biotec) using a 4x objective for the fluorescent proteins or 1.3x objective for autofluorescence imaging. The ClearMap pipeline was used as previously described to map the data to the Allen Brain Reference Atlas. All signal mapped to thalamus was summed and the percent of signal in each nucleus was calculated for each animal.

Retrograde mapping

Two weeks post injection, mice were euthanized by intracardial perfusion with 1× PBS followed by 4% paraformaldehyde. Brains were post-fixed in 4% paraformaldehyde overnight at 4 °C. Serial coronal sections (50um) were collected and stained with NeuroTrace 640/660 (ThermoFisher Scientific). Imaging was performed with an AZ100 automated slide scanning microscope using a 4x objective (Nikon, 0.4 NA). Image processing, registration to the Allen Brain Reference Atlas, and automated counting were performed as previously described[47]. Cell counts per animal were summed over anatomical regions or binned according to their mapped position for comparative analysis.

Two-photon imaging and analysis

All behavioral training and habituation were conducted as described above. Training did not commence until at least 8 weeks post viral injection. A behavioral assembly similar to those described for behavior was placed on a modified 2p microscope (Bruker) for calcium imaging experiments. A 25x water immersion objective (Olympus,1 NA) was used with a mode-locked Ti:sapphire laser (Verdi 18W, Coherent) at 920 nm. Images were collected with Prairie View software (Bruker) at 64 Hz and averaged every 4 images for an effective sampling rate of 16 Hz. The pial surface of the brain surface was identified at the beginning of each imaging session, and fields of view were selected at least 300um below the pial surface. Voltage recordings of the encoder and solenoid were also collected with Prairie View. The behavioral code was run from a separate computer, and all behavioral components recorded. The encoder signal was used to align the imaging to the behavioral recordings. Motion correction and signal extraction was performed using CNMF as previously described[50] with an autoregressive process p of 2. For analysis of the whole session, the $\Delta F/F$ or deconvolved events were z-scored over the whole session for individual neurons and then aggregated across animals for further analysis. For analysis of trials or pulls, the $\Delta F/F$ or deconvolved events were z-scored to signal 2-1.5 s prior to the movement event for each neuron. ROC classification was performed by calculating the approximate integral using the trapezoidal method for 100 ms bins starting 2s before pull max and extending 2s after and z-scored to the first five bins (-2 to -1.5 from pull max). Neurons with at least two bins of the 3 proceeding and the 3 preceding the pull max (total of 600 ms) with a z-score greater than 2 or -2 were classified as CT up or CT down respectively. All other neurons were classified as not modulated.

Optogenetic manipulations

All behavioral training and habituation were conducted as described above. On the days of optogenetic manipulations, a plastic fiberoptic patch cord (960 um core; 0.63 NA) ending in a metal ferrule (Doric) was placed directly over the cranial window. A multichannel LED driver (Doric) was used with 465nm central wavelength connectorized LED (Doric; ~35 mW). For closed-loop experiments, a pulse was sent at trial start on one third of trials to the driver to trigger light delivery as programmed in Doric Neuroscience Studio software. Light was delivered for 400 ms at 20hz with a pulse width of 10ms. For open-loop experiments, light delivery was triggered using a random number generator to give light for 10% of the session. Light was delivered for 1.2 s at 20 hz.

Histology and imaging

Images of CaMPARI photoconversion were obtained from mice trained as described above. Images of GCaMP expression were obtained from mice used for imaging once all training was complete. Mice were euthanized by intracardial perfusion with 1× PBS followed by 4% paraformaldehyde. Brains were post-fixed in 4% paraformaldehyde overnight at 4 °C. Coronal sections (50um) were cut with a vibratome. DAPI was used as a counterstain. For CaMPARI slices, imaging was performed with a confocal microscope (Zeiss 880) with a 20x objective within

a week of mounting. For GCaMP slices, imaging was performed with an AZ100 automated slide scanning microscope using a 4x objective (Nikon, 0.4 NA).

Statistical Analysis

Statistical parameters, statistical tests, and statistical significance are reported throughout. Significance is defined as $P<0.05$ with significance annotations of $*P < 0.05$, $**P < 0.01$, $***P < 0.001$ and $****P < 0.0001$. All statistical analysis was performed using R, GraphPad Prism, Python, or MATLAB.

REFERENCES

1 Arber, S. Motor circuits in action: specification, connectivity, and function. *Neuron* **74**, 975-989 (2012). https://doi.org:10.1016/j.neuron.2012.05.011

2 Svoboda, K. & Li, N. Neural mechanisms of movement planning: motor cortex and beyond. *Curr Opin Neurobiol* **49**, 33-41 (2018). https://doi.org:10.1016/j.conb.2017.10.023

3 Arber, S. & Costa, R. M. Connecting neuronal circuits for movement. *Science* **360**, 1403-1404 (2018). https://doi.org:10.1126/science.aat5994

4 Jeong, M. *et al.* Comparative three-dimensional connectome map of motor cortical projections in the mouse brain. *Sci Rep* **6**, 20072 (2016). https://doi.org:10.1038/srep20072

5 Whishaw, I. Q., Pellis, S. M., Gorny, B., Kolb, B. & Tetzlaff, W. Proximal and distal impairments in rat forelimb use in reaching follow unilateral pyramidal tract lesions. *Behav Brain Res* **56**, 59-76 (1993). https://doi.org:10.1016/0166-4328(93)90022-i

6 Whishaw, I. Q., Pellis, S. M., Gorny, B. P. & Pellis, V. C. The impairments in reaching and the movements of compensation in rats with motor cortex lesions: an endpoint, videorecording, and movement notation analysis. *Behav Brain Res* **42**, 77-91 (1991). https://doi.org:10.1016/s0166-4328(05)80042-7

7 Lawrence, D. G. & Kuypers, H. G. The functional organization of the motor system in the monkey. I. The effects of bilateral pyramidal lesions. *Brain* **91**, 1-14 (1968). https://doi.org:10.1093/brain/91.1.1

8 Evarts, E. V. Pyramidal tract activity associated with a conditioned hand movement in the monkey. *J Neurophysiol* **29**, 1011-1027 (1966). https://doi.org:10.1152/jn.1966.29.6.1011

9 Karni, A. *et al.* Functional MRI evidence for adult motor cortex plasticity during motor skill learning. *Nature* **377**, 155-158 (1995). https://doi.org:10.1038/377155a0

10 Matsuzaka, Y., Picard, N. & Strick, P. L. Skill representation in the primary motor cortex after long-term practice. *J Neurophysiol* **97**, 1819-1832 (2007). https://doi.org:10.1152/jn.00784.2006

11 Kawai, R. *et al.* Motor cortex is required for learning but not for executing a motor skill. *Neuron* **86**, 800-812 (2015). https://doi.org:10.1016/j.neuron.2015.03.024

12 Miri, A. *et al.* Behaviorally Selective Engagement of Short-Latency Effector Pathways by Motor Cortex. *Neuron* **95**, 683-696 e611 (2017). https://doi.org:10.1016/j.neuron.2017.06.042

13 Yang, G., Pan, F. & Gan, W. B. Stably maintained dendritic spines are associated with lifelong memories. *Nature* **462**, 920-924 (2009). https://doi.org:10.1038/nature08577

14 Fu, M., Yu, X., Lu, J. & Zuo, Y. Repetitive motor learning induces coordinated formation of clustered dendritic spines in vivo. *Nature* **483**, 92-95 (2012). https://doi.org:10.1038/nature10844

15 Peters, A. J., Chen, S. X. & Komiyama, T. Emergence of reproducible spatiotemporal activity during motor learning. *Nature* **510**, 263-267 (2014). https://doi.org:10.1038/nature13235

16 Xu, T. *et al.* Rapid formation and selective stabilization of synapses for enduring motor memories. *Nature* (2009). https://doi.org:10.1038/nature08389

17 Harms, K. J., Rioult-Pedotti, M. S., Carter, D. R. & Dunaevsky, A. Transient spine expansion and learning-induced plasticity in layer 1 primary motor cortex. *J Neurosci* **28**, 5686-5690 (2008). https://doi.org:10.1523/JNEUROSCI.0584-08.2008

18 Greenough, W. T., Larson, J. R. & Withers, G. S. Effects of unilateral and bilateral training in a reaching task on dendritic branching of neurons in the rat motor-sensory forelimb cortex. *Behav Neural Biol* **44**, 301-314 (1985).

19 Withers, G. S. & Greenough, W. T. Reach training selectively alters dendritic branching in subpopulations of layer II-III pyramids in rat motor-somatosensory forelimb cortex. *Neuropsychologia* **27**, 61-69 (1989). https://doi.org:10.1016/0028-3932(89)90090-0

20 Gloor, C., Luft, A. R. & Hosp, J. A. Biphasic plasticity of dendritic fields in layer V motor neurons in response to motor learning. *Neurobiology of learning and memory* (2015).

21 Wang, L., Conner, J. M., Rickert, J. & Tuszynski, M. H. Structural plasticity within highly specific neuronal populations identifies a unique parcellation of motor learning in the adult brain. *Proc Natl Acad Sci U S A* **108**, 2545-2550 (2011). https://doi.org:10.1073/pnas.1014335108

22 Chen, S. X., Kim, A. N., Peters, A. J. & Komiyama, T. Subtype-specific plasticity of inhibitory circuits in motor cortex during motor learning. *Nature neuroscience* (2015). https://doi.org:10.1038/nn.4049

23 Peters, A. J., Lee, J., Hedrick, N. G., O'Neil, K. & Komiyama, T. Reorganization of corticospinal output during motor learning. *Nat Neurosci* **20**, 1133-1141 (2017). https://doi.org:10.1038/nn.4596

24 Laubach, M., Wessberg, J. & Nicolelis, M. A. Cortical ensemble activity increasingly predicts behaviour outcomes during learning of a motor task. *Nature* **405**, 567-571 (2000). https://doi.org:10.1038/35014604

25 Huber, D. *et al.* Multiple dynamic representations in the motor cortex during sensorimotor learning. *Nature* **484**, 473-478 (2012). https://doi.org:10.1038/nature11039

26 Masamizu, Y. *et al.* Two distinct layer-specific dynamics of cortical ensembles during learning of a motor task. *Nat Neurosci* **17**, 987-994 (2014). https://doi.org:10.1038/nn.3739

27 Nelson, A., Abdelmesih, B. & Costa, R. M. Corticospinal populations broadcast complex motor signals to coordinated spinal and striatal circuits. *Nat Neurosci* **24**, 1721-1732 (2021). https://doi.org:10.1038/s41593-021-00939-w

28 Yao, Z. *et al.* A transcriptomic and epigenomic cell atlas of the mouse primary motor cortex. *Nature* **598**, 103-110 (2021). https://doi.org:10.1038/s41586-021-03500-8

29 Network, B. I. C. C. A multimodal cell census and atlas of the mammalian primary motor cortex. *Nature* **598**, 86-102 (2021). https://doi.org:10.1038/s41586-021-03950-0

30 Bakken, T. E. *et al.* Comparative cellular analysis of motor cortex in human, marmoset and mouse. *Nature* **598**, 111-119 (2021). https://doi.org:10.1038/s41586-021-03465-8

31 Park, J. *et al.* Motor cortical output for skilled forelimb movement is selectively distributed across projection neuron classes. *Sci Adv* **8**, eabj5167 (2022). https://doi.org:10.1126/sciadv.abj5167

32 Warriner, C. L., Fageiry, S., Saxena, S., Costa, R. M. & Miri, A. Motor cortical influence relies on task-specific activity covariation. *bioRxiv*, 2022.2002.2009.479479 (2022). https://doi.org:10.1101/2022.02.09.479479

33 Fosque, B. F. *et al.* Neural circuits. Labeling of active neural circuits in vivo with designed calcium integrators. *Science (New York, N.Y.)* **347**, 755-760 (2015). https://doi.org:10.1126/science.1260922

34 DeNardo, L. A. *et al.* Temporal evolution of cortical ensembles promoting remote memory retrieval. *Nat Neurosci* **22**, 460-469 (2019). https://doi.org:10.1038/s41593-018-0318-7

35 Wang, W. *et al.* A light- and calcium-gated transcription factor for imaging and manipulating activated neurons. *Nat Biotechnol* (2017). https://doi.org:10.1038/nbt.3909

36 Lee, D., Hyun, J. H., Jung, K., Hannan, P. & Kwon, H. B. A calcium- and light-gated switch to induce gene expression in activated neurons. *Nature Biotechnology* **35**, 858-+ (2017). https://doi.org:10.1038/nbt.3902

37 Kim, C. K. *et al.* A Molecular Calcium Integrator Reveals a Striatal Cell Type Driving Aversion. *Cell* **183**, 2003-2019 e2016 (2020). https://doi.org:10.1016/j.cell.2020.11.015

38 Tennant, K. A. *et al.* The organization of the forelimb representation of the C57BL/6 mouse motor cortex as defined by intracortical microstimulation and cytoarchitecture. *Cereb Cortex* **21**, 865-876 (2011). https://doi.org:10.1093/cercor/bhq159

39 Hira, R. *et al.* In vivo optogenetic tracing of functional corticocortical connections between motor forelimb areas. *Front Neural Circuits* **7**, 55 (2013). https://doi.org:10.3389/fncir.2013.00055

40 Canavan, A. G., Nixon, P. D. & Passingham, R. E. Motor learning in monkeys (Macaca fascicularis) with lesions in motor thalamus. *Exp Brain Res* **77**, 113-126 (1989). https://doi.org:10.1007/BF00250573

41 Bosch-Bouju, C., Hyland, B. I. & Parr-Brownlie, L. C. Motor thalamus integration of cortical, cerebellar and basal ganglia information: implications for normal and parkinsonian conditions. *Front Comput Neurosci* **7**, 163 (2013). https://doi.org:10.3389/fncom.2013.00163

42 Johnson, F. & Bottjer, S. W. Induced cell death in a thalamic nucleus during a restricted period of zebra finch vocal development. *J Neurosci* **13**, 2452-2462 (1993).

43 Chi, J., Crane, A., Wu, Z. & Cohen, P. Adipo-Clear: A Tissue Clearing Method for Three-Dimensional Imaging of Adipose Tissue. *J Vis Exp* (2018). https://doi.org:10.3791/58271

44 Renier, N. *et al.* Mapping of Brain Activity by Automated Volume Analysis of Immediate Early Genes. *Cell* **165**, 1789-1802 (2016). https://doi.org:10.1016/j.cell.2016.05.007

45 Yamawaki, N. & Shepherd, G. M. Synaptic circuit organization of motor corticothalamic neurons. *J Neurosci* **35**, 2293-2307 (2015). https://doi.org:10.1523/JNEUROSCI.4023-14.2015

46 Munoz-Castaneda, R. *et al.* Cellular anatomy of the mouse primary motor cortex. *Nature* **598**, 159-166 (2021). https://doi.org:10.1038/s41586-021-03970-w

47 Botta, P. *et al.* An Amygdala Circuit Mediates Experience-Dependent Momentary Arrests during Exploration. *Cell* **183**, 605-619 e622 (2020). https://doi.org:10.1016/j.cell.2020.09.023

48 Sauerbrei, B. A. *et al.* Cortical pattern generation during dexterous movement is input-driven. *Nature* **577**, 386-391 (2020). https://doi.org:10.1038/s41586-019-1869-9

49 Tanaka, Y. H. *et al.* Thalamocortical Axonal Activity in Motor Cortex Exhibits Layer-Specific Dynamics during Motor Learning. *Neuron* **100**, 244-258 e212 (2018). https://doi.org:10.1016/j.neuron.2018.08.016

50 Pnevmatikakis, E. A. *et al.* Simultaneous Denoising, Deconvolution, and Demixing of Calcium Imaging Data. *Neuron* **89**, 285-299 (2016). https://doi.org:10.1016/j.neuron.2015.11.037

51 Mittmann, W. *et al.* Two-photon calcium imaging of evoked activity from L5 somatosensory neurons in vivo. *Nat Neurosci* **14**, 1089-1093 (2011). https://doi.org:10.1038/nn.2879

52 Hrvatin, S. *et al.* Single-cell analysis of experience-dependent transcriptomic states in the mouse visual cortex. *Nat Neurosci* **21**, 120-129 (2018). https://doi.org:10.1038/s41593-017-0029-5

Figure 1

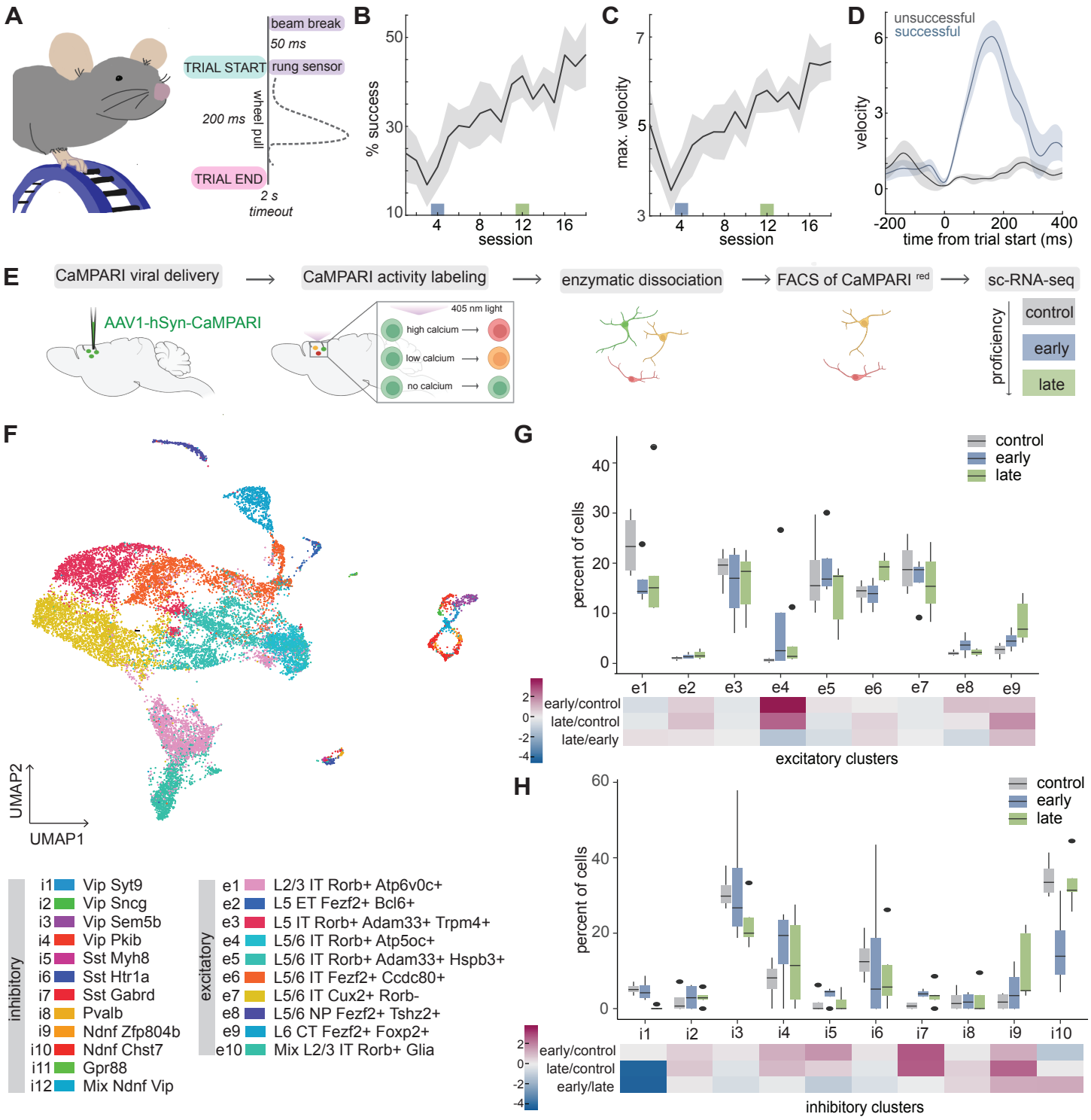
A
beam break
50 ms
TRIAL START
rung sensor
200 ms
wheel pull
TRIAL END
2 s
timeout
B
% success
session
C
max. velocity
session
D
unsuccessful
successful
velocity
time from trial start (ms)
E
CaMPARI viral delivery
CaMPARI activity labeling
enzymatic dissociation
FACS of CaMPARI red
sc-RNA-seq
AAV1-hSyn-CaMPARI
405 nm light
high calcium
low calcium
no calcium
proficiency
control
early
late
F
UMAP2
UMAP1
inhibitory
i1 Vip Syt9
i2 Vip Sncg
i3 Vip Sem5b
i4 Vip Pkib
i5 Sst Myh8
i6 Sst Htr1a
i7 Sst Gabrd
i8 Pvalb
i9 Ndnf Zfp804b
i10 Ndnf Chst7
i11 Gpr88
i12 Mix Ndnf Vip
excitatory
e1 L2/3 IT Rorb+ Atp6v0c+
e2 L5 ET Fezf2+ Bcl6+
e3 L5 IT Rorb+ Adam33+ Trpm4+
e4 L5/6 IT Rorb+ Atp5oc+
e5 L5/6 IT Rorb+ Adam33+ Hspb3+
e6 L5/6 IT Fezf2+ Ccdc80+
e7 L5/6 IT Cux2+ Rorb-
e8 L5/6 NP Fezf2+ Tshz2+
e9 L6 CT Fezf2+ Foxp2+
e10 Mix L2/3 IT Rorb+ Glia
G
control
early
late
percent of cells
e1 e2 e3 e4 e5 e6 e7 e8 e9
early/control
late/control
late/early
excitatory clusters
H
control
early
late
percent of cells
i1 i2 i3 i4 i5 i6 i7 i8 i9 i10
early/control
late/control
early/late
inhibitory clusters

Figure 1. M1 active cell type enrichment during training of a motor task

A Schematic of wheel pulling task, left. Schematic of trial structure, right. **B,C** Percent success **(B)** and maximum velocity of all trials **(C)** during 18 consecutive training sessions; N=6. Early and late training are denoted by blue and green boxes, respectively; p=0.0104 **(B)** and p=0.0182 **(C)**, one way ANOVA, time; p=0.0336 **(B)** and p=0.0569 **(C)** early v. late training, one-way ANOVA. **D** Velocity of successful (blue) and unsuccessful trials (gray) on day 4 (early training). **E** Outline of labeling, sorting, and sc-RNAseq strategy. **F** Aggregate UMAP of all sc-RNA-seq runs. **G,H** Percent of excitatory **(G)** or inhibitory **(H)** neurons present from each clusters at each timepoint, top; Gray, control; Blue, early training; Green, late training. Fold change between the early and control, late and control, and early and late, bottom.

Figure 2

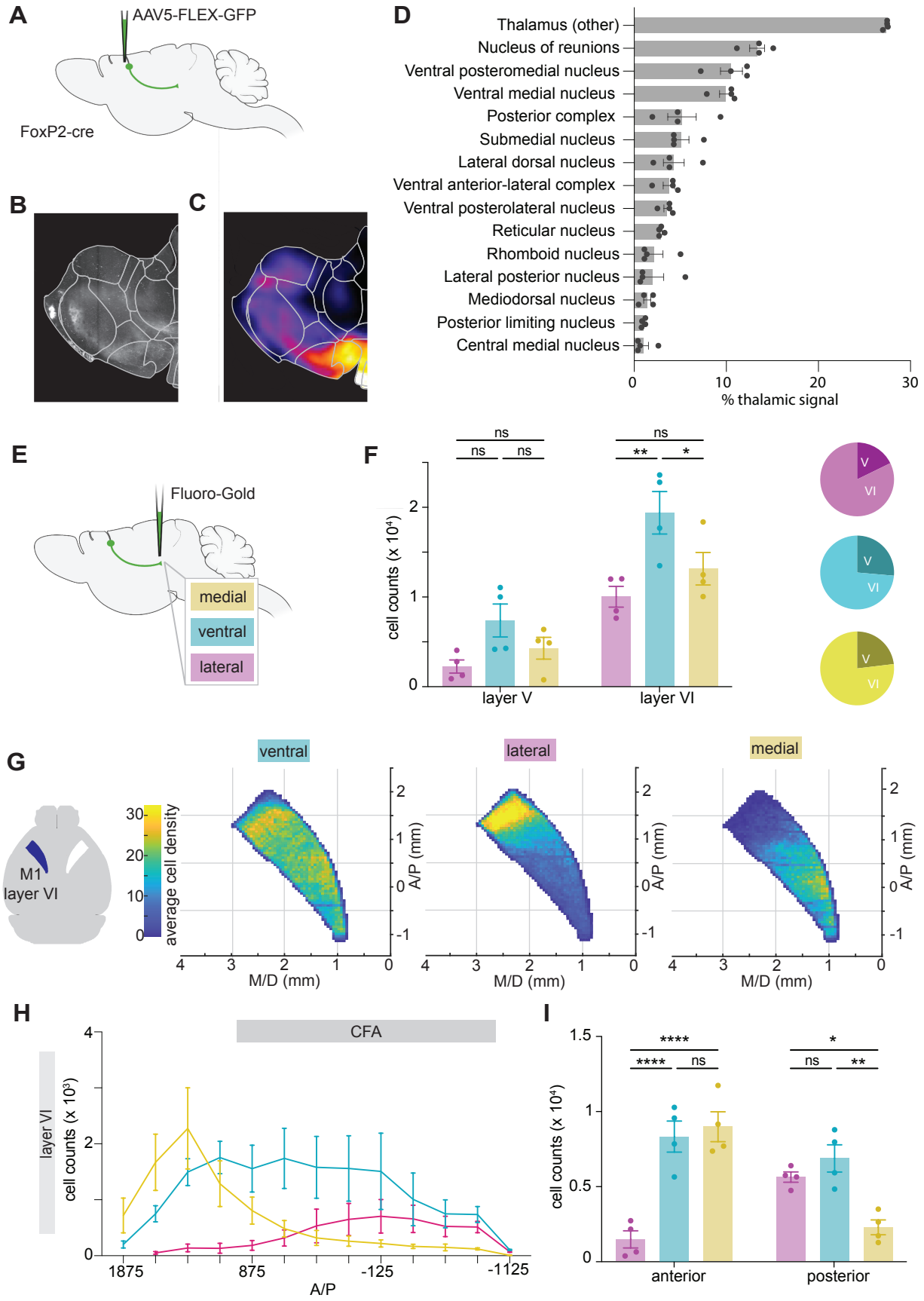
A
AAV5-FLEX-GFP
FoxP2-cre
B
C
D
Thalamus (other)
Nucleus of reunions
Ventral posteromedial nucleus
Ventral medial nucleus
Posterior complex
Submedial nucleus
Lateral dorsal nucleus
Ventral anterior-lateral complex
Ventral posterolateral nucleus
Reticular nucleus
Rhomboid nucleus
Lateral posterior nucleus
Mediodorsal nucleus
Posterior limiting nucleus
Central medial nucleus
0
10
20
30
% thalamic signal
E
Fluoro-Gold
medial
ventral
lateral
F
ns
ns
ns
ns
**
*
cell counts (x 10⁴)
layer V
layer VI
V
VI
G
M1
layer VI
average cell density
ventral
lateral
medial
A/P (mm)
M/D (mm)
H
CFA
layer VI
cell counts (x 10³)
1875
875
-125
-1125
A/P
I
****
****
ns
*
ns
**
cell counts (x 10⁴)
anterior
posterior

Figure 2. $M1^{CT}$ connection logic to thalamus

A Schematic of $M1^{CT}$ projection mapping in thalamus from M1 in FoxP2-cre mice. **B** Max projection of representative $M1^{CT}$ projections in thalamus; mCherry labeling. **C** Heatmap of thalamic signal; N=4. **D** Thalamic regions with greater than 1% of total thalamic signal; N=4; error bars, SEM. **E** Schematic of retrograde labeling of $M1^{CT}$ neurons from three regions of thalamus: medial, ventral, and lateral. **F** Left, number of $M1^{CT}$ neurons labeled from each thalamic region in both M1 layer V and layer VI. Right, percent of total signal in either cortical layer; purple, lateral; cyan, ventral; medial, yellow, N=4 per group; two-way ANOVA, p=0.0020 (lateral v. ventral, layer VI); p=0.0400 (ventral v. medial, layer VI). **G** Distribution of cell density of layer VI $M1^{CT}$ from each thalamic target; left, schematic of M1 layer VI, left hemisphere, blue, mapped; N=4 per group. **H** Number of $M1^{CT}$ neurons labeled in layer VI from each thalamic region along the anterior/posterior axis; 0=Bregma; N=4 per group; error bars, SEM. **I** Aggregate cell counts of layer VI $M1^{CT}$ neurons labeled from each thalamic target in anterior or posterior regions of M1; N=4 per group; error bars, SEM; two-way ANOVA, p<0.001 (anterior, medial v. lateral); p=0.0173 (posterior, medial v. lateral).

Figure 3

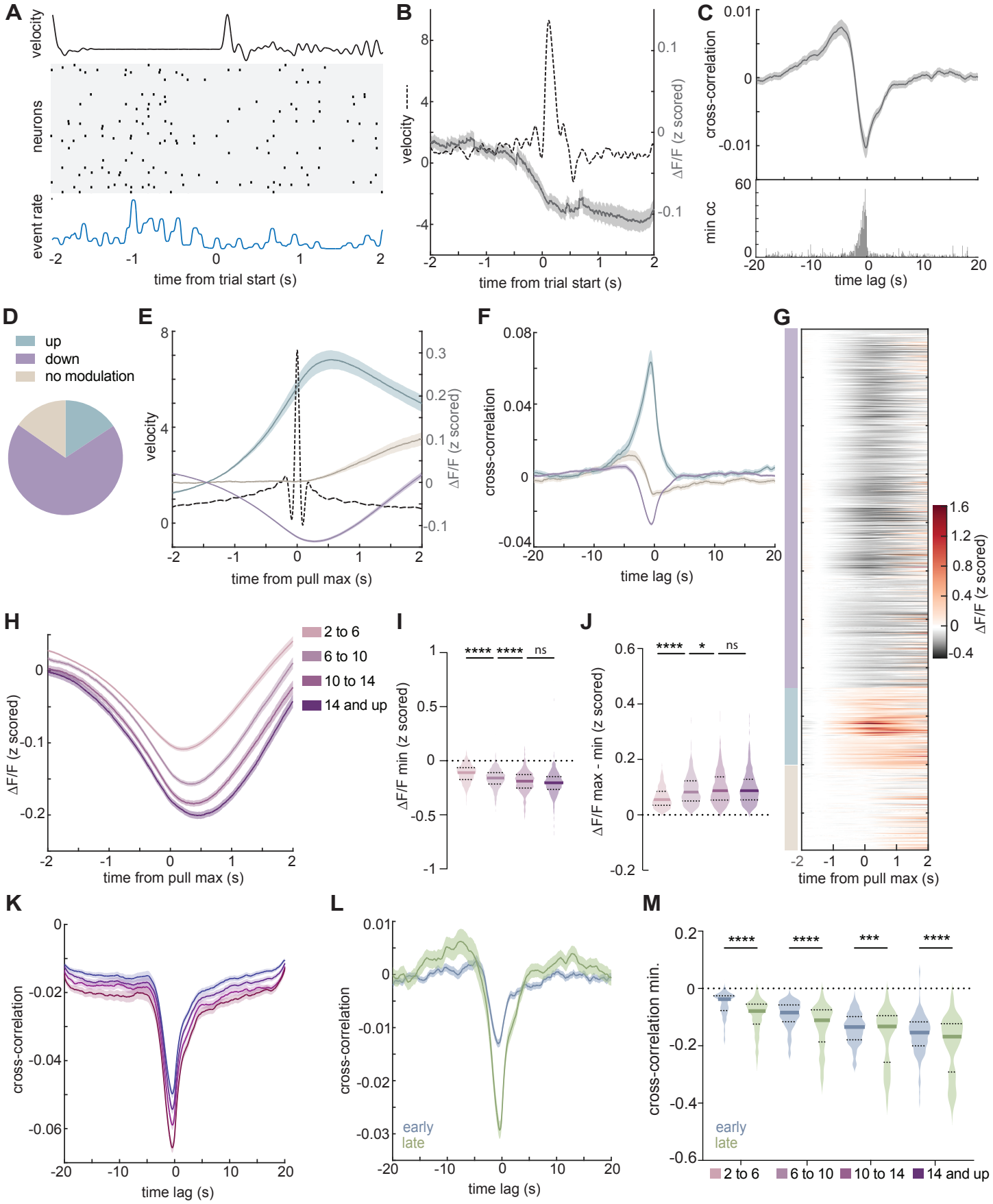
A
velocity
neurons
event rate
time from trial start (s)
B
velocity
ΔF/F (z scored)
time from trial start (s)
C
cross-correlation
min cc
time lag (s)
D
up
down
no modulation
E
velocity
ΔF/F (z scored)
time from pull max (s)
F
cross-correlation
time lag (s)
G
ΔF/F (z scored)
time from pull max (s)
H
2 to 6
6 to 10
10 to 14
14 and up
ΔF/F (z scored)
time from pull max (s)
I
ΔF/F min (z scored)
**** **** ns
J
ΔF/F max - min (z scored)
**** * ns
K
cross-correlation
time lag (s)
L
cross-correlation
early
late
time lag (s)
M
cross-correlation min.
**** **** *** ****
early
late
2 to 6
6 to 10
10 to 14
14 and up

Figure 3. $M1^{CT}$ neurons are suppressed during movement

A Single trial example of $M1^{CT}$ activity; top, wheel velocity; middle; raster plot of all units (N=53); bottom, aggregate event rate; 0=trial start. **B** Z-scored ∆F/F during successful trials over all sessions; mean, solid gray line; shaded area, SEM; Wheel velocity during same trials, dotted line; n=1078; N=4; **C** Top, cross-correlation of Z-scored calcium ∆F/F to wheel velocity for whole session wheel pulls; mean, solid gray line; shaded area, SEM; bottom, binned cross-correlation minimum values at corresponding lags; 50ms bins. **D.** ROC based classification of all units across sessions based on activity during wheel pulls. **E,F** Z-scored ∆F/F **(E)** and cross-correlation to wheel velocity for whole session **(F)** of each group during wheel pulls; solid lines, mean; shaded areas, SEM; wheel velocity during pulls, dotted line in **E**. 0=pull velocity max. **G** Z-scored ∆F/F of all units averaged over all wheel pulls; groups denoted on left. **H** Z-scored ∆F/F of wheel pulls of increasing velocities for down modulated neurons; solid line, mean; shaded area, SEM. **I,J** Distribution of z-scored ∆F/F minimum during wheel pulls **(I)** or the difference in z-scored ∆F/F maximum and minimum before and during wheel pulls **(J)** of down modulated neurons; colors as in **H**. Thick solid line, mean; thin lines, quartiles. One-way ANOVA, multiple comparisons; $p<0.0001$, 2 to 6 v. 6 to 10 and 6 to 10 v 10 to 14; $p=0.0553$, 10 to 14 v 14 and up **(I)**, $p<0.0001$, 2 to 6 v 6 to 10; $p=0.230$, 6 to 10 v 10 to 14; $p=0.9937$, 10 to 14 v 14 and up **(J)**. **K,L** cross-correlation to wheel velocity for trials **(K)** and whole session **(L)** for wheel pulls of each velocity bin group **(K)** or early (blue) and late (green) training sessions **(L)** in down modulated neurons; solid line, mean; shaded area, SEM. **M** Distribution of minimum cross-correlation to wheel velocity during pulls of increasing velocity in early (blue) or late (green) sessions of down modulated neurons; thick, line, mean; thin lines, quartiles. Early v. late comparisons, one-way ANOVA, multiple comparisons, $p<0.001$, 2 to 6, 6 to 10, and 14 and up; $p=0.005$, 10 to 14.

Figure 4

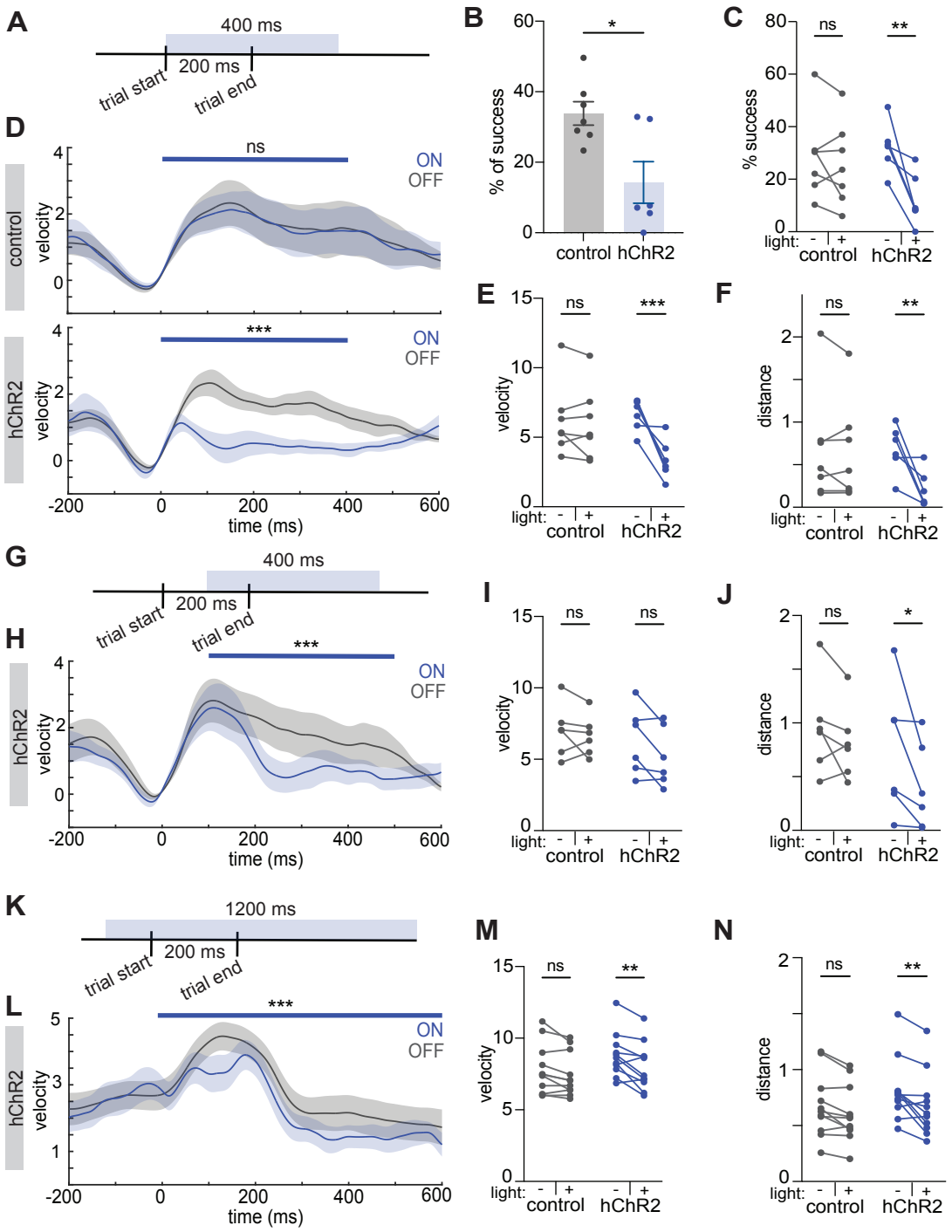
A
400 ms
200 ms
trial start
trial end
B
% of success
control
hChR2
C
% success
light:
control
hChR2
D
control
hChR2
velocity
ns
***
ON
OFF
time (ms)
E
velocity
F
distance
G
H
I
J
K
1200 ms
L
M
N

Figure 4. M1^{CT} activity disruption perturbs movement execution

A, G, K Schematic of optogenetic light delivery for closed loop at trial start (**A**), closed loop at velocity max (**G**), and open loop trials with light on 100 ms preceding pull start (**K**) for wheel turning task. **B** Percent of successful trials with light on; control, gray; hChR2, blue; error bars, SEM; two-tailed unpaired t-test, p=0.0119**.** For B-J: N=7**,** control group; N=6, hChR2 group. Each point is average of all light delivery sessions. **C** Percentage of trials that are successful for each animal with light on or off in each group; error bars, SEM; two-way ANOVA, multiple comparisons; p=0.7031, control; p=0.0014, hChR2**. D** Velocity traces of all trials from control, top, and hChR2, bottom, animals during light, blue, and no light trials, gray; 0=trial start; blue bar denotes time of light, p>0.9999 (control), p<0.0001 (hChR2), time x condition, two way ANOVA; solid line, mean; shaded area, SEM. **E, I, M.** Maximum velocity of all trials for each animal with light on or off in each group; error bars, SEM; two-way ANOVA, multiple comparisons. **E**, p=0.8713 (control), p=0.0003 (hChR2)**; I**, p=0.7329, (control), p=0.0789 (hChR2); **M**, p=0.1558 (control, p=0.0016 (hChR2)**;** N=7 for both groups for H-J. N=11 for both groups for L-N **F,J,N** Wheel distance traveled during all trials for each animal with light on or off for each group; error bars, SEM; two way ANOVA, multiple comparisons; **F**, p=0.9511, (control), p=0.0027, hChR2**; J**, p=0.5128 (control), p=0.0406 (hChR2); **N**, p=0.0708 (control), p=0.0011 (hChR2). **H,L** Velocity traces of all trials from hChR2 animals during light, blue, and no light trials, gray; 0=trial start; blue bar denotes time of light; p=0.0003 **(H)** and p<0.0001 **(L)**, time x condition, two way ANOVA; solid line, mean; shaded area, SEM.

Extended Data Figure 1

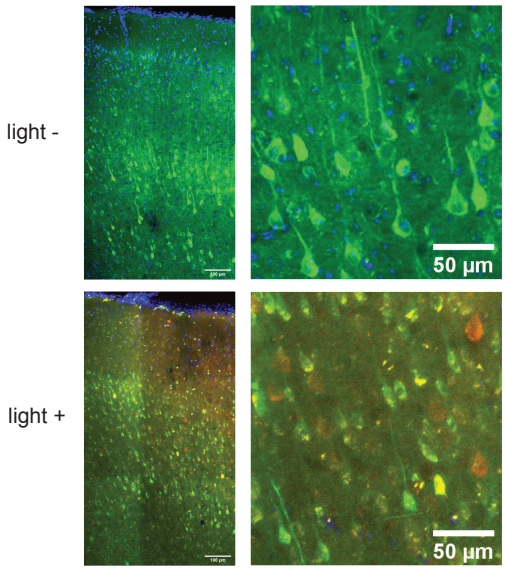

Extended Data Figure 1. CaMPARI expression in M1 neurons

Representative images of CaMPARI levels in mice performing the wheel turning task in the absence (top) and presence (bottom) of photoconversion light. Right panels are zoom insets of left.

Extended Data Figure 2

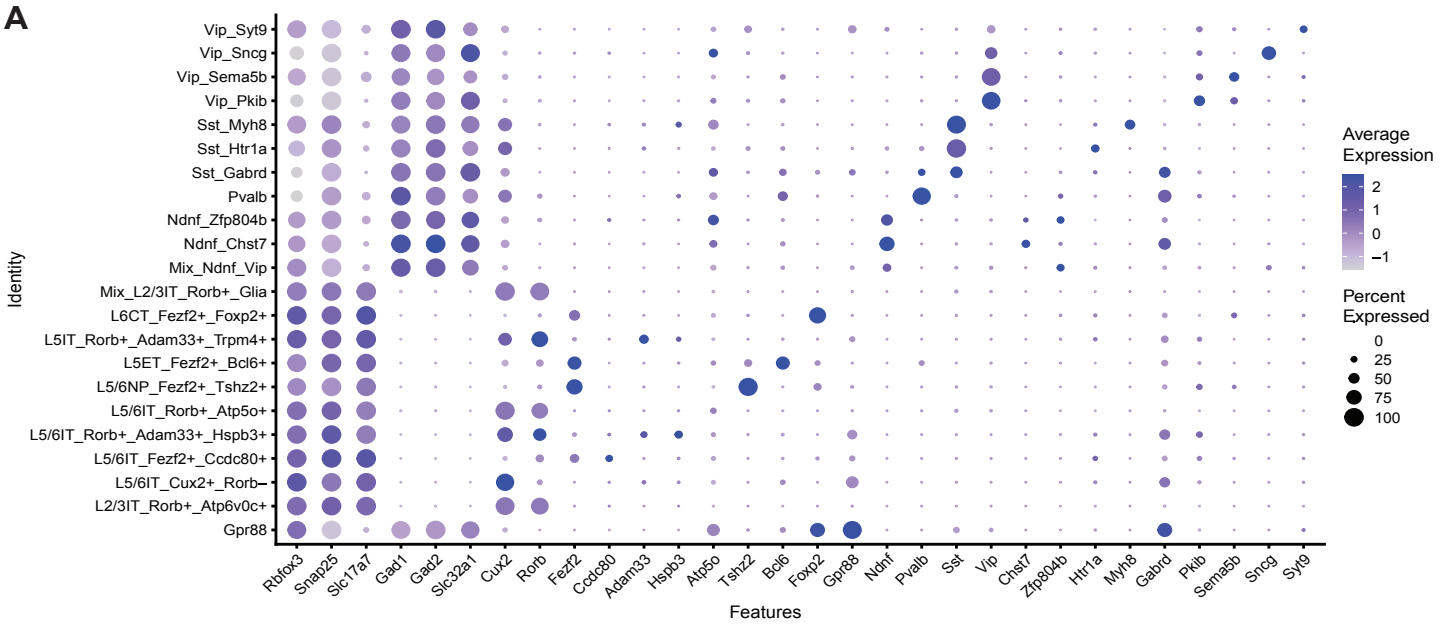

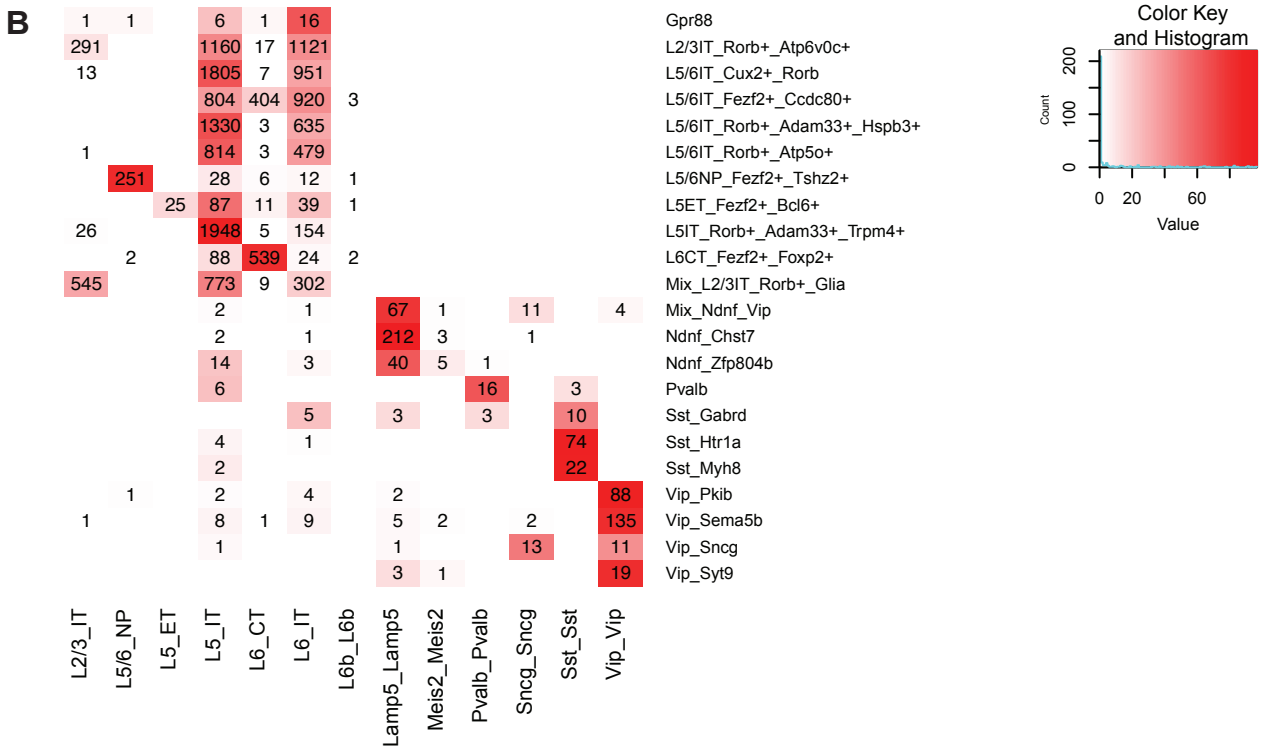

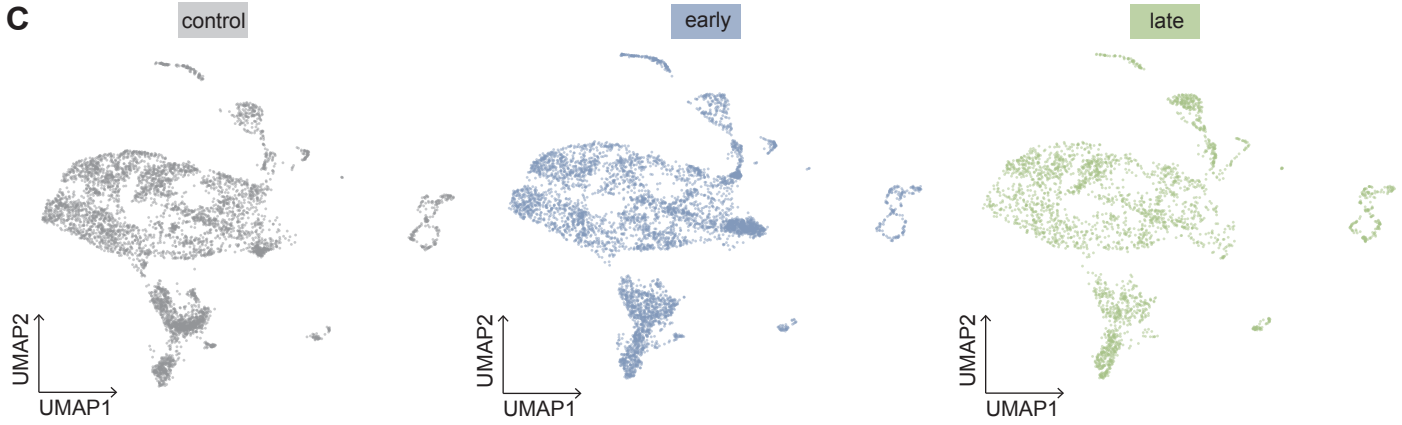

Extended Data Figure 2. Gene expression and mapping of single cell RNA sequencing

A Average, purple gradient, and percent expression, size of dot, of marker genes in each cluster. **B** Number of cells mapped from clusters identified in aggregate sc-RNAseq runs to clusters of the M1 cell type atlas. **C** UMAPs of scRNA-seq runs from each condition mapped to M1 cell type atlas; gray, control; blue, early training; green, late training.

Extended Data Figure 3

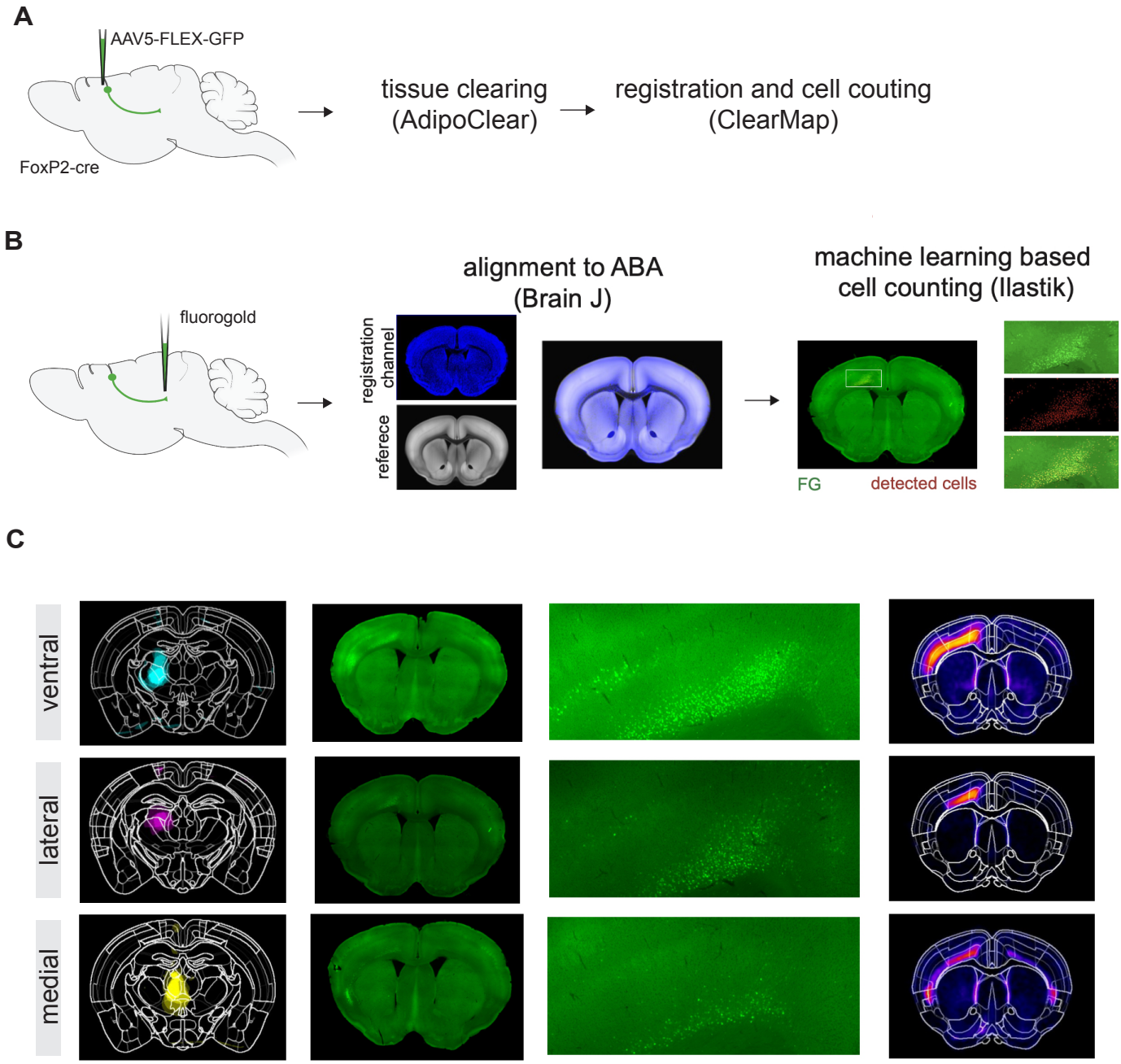

Extended Data Figure 3. Anatomical approaches for mapping $M1^{CT}$ neurons and projections

A Schematic of workflow for $M1^{CT}$ projection mapping. **B** Schematic of workflow for $M1^{CT}$ retrograde labeling and mapping. **C** Summary of each thalamic injection site; left, heatmap of injection site, N=4; middle, representative images of fluorogold labeling in M1, whole slice and zoomed inset of M1; right, heatmaps of fluorogold signal, N=4.

Extended Data Figure 4

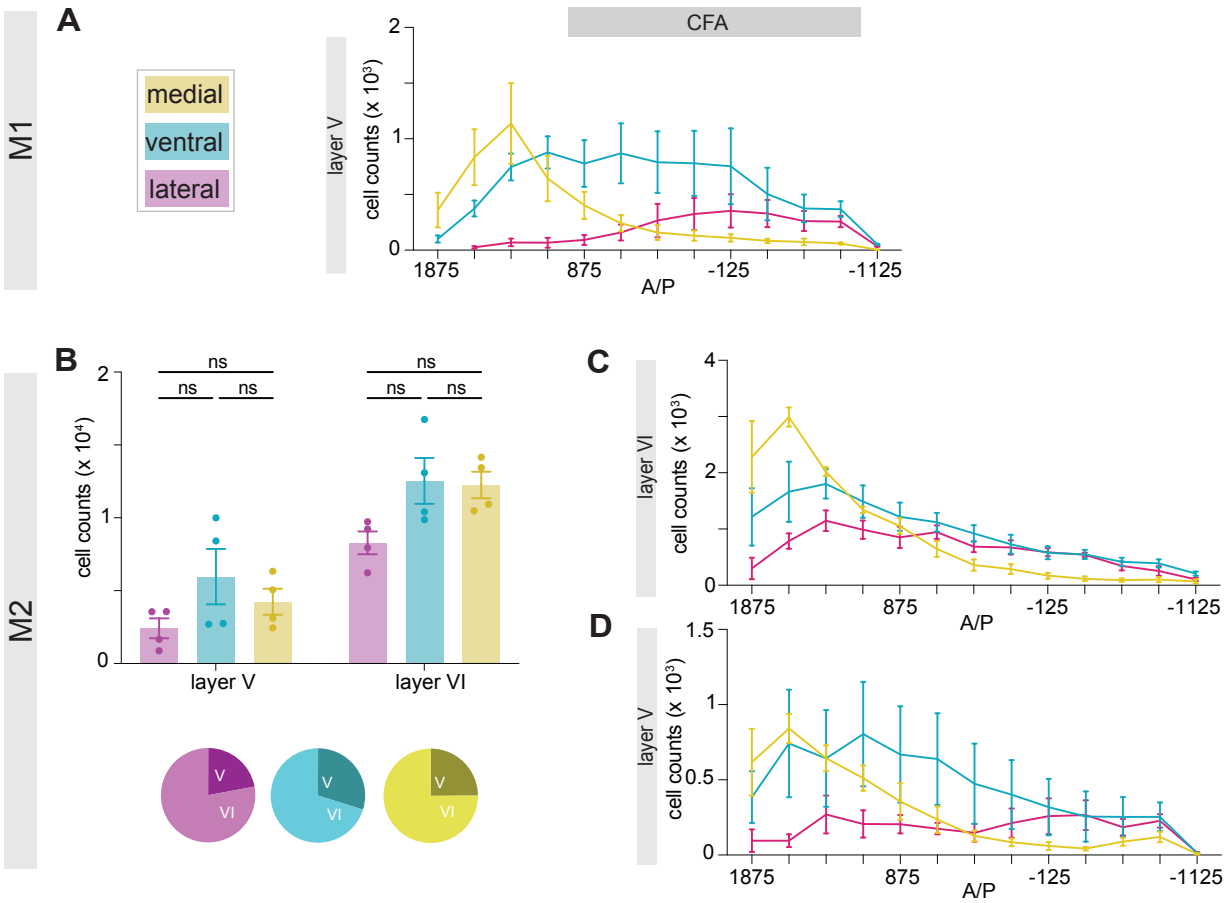

Extended Data Figure 4 (cont.)

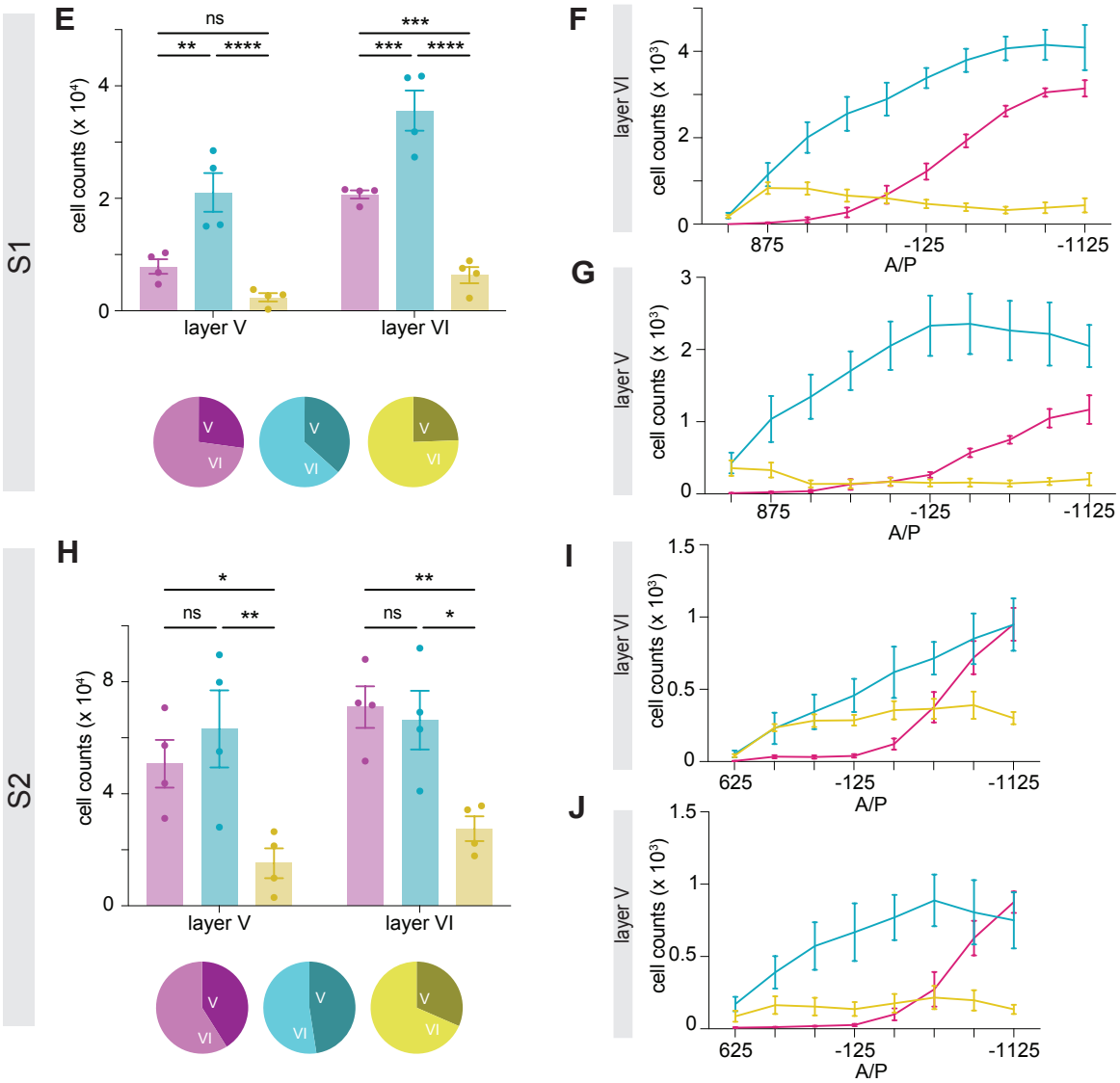

Extended Data Figure 4. Distribution of $M1^{CT}$ neurons in motor cortex

A Number of $M1^{CT}$ neurons labeled in layer V from each thalamic region along the anterior/posterior axis; 0=Bregma; N=4 per group; error bars, SEM. **B,E,H** Top, number of corticothalamic neurons labeled from each thalamic region in both layer V and layer VI of the indicated region (M2, S1 or S2). Bottom, percent of total signal in either cortical layer; purple, lateral; cyan, ventral; medial, yellow, N=4 per group; two-way ANOVA, *: $p <= 0.05$; **: $p <= 0.01$; ***: $p <= 0.001$. **C,F,I** Number of corticothalamic neurons labeled in layer VI from each thalamic region at each indicated region M2, S1 or S2) along the anterior/posterior axis; 0=Bregma; N=4 per group; error bars, SEM. **D,G,J** Number of corticothalamic neurons labeled in layer V from each thalamic region at each indicated region M2, S1 or S2) along the anterior/posterior axis; 0=Bregma; N=4 per group; error bars, SEM.

Extended Data Figure 5

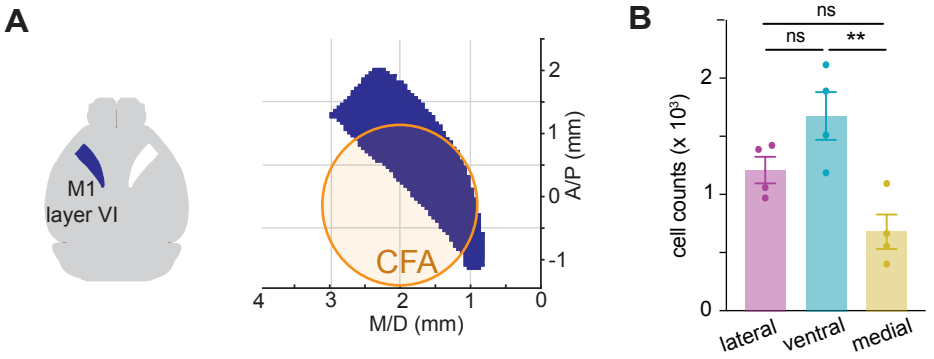

Extended Data Figure 5. Enrichment of $M1^{CT}$ neurons projecting to subregions of thalamus within CFA

A Schematic of CFA relative to layer V of M1 **B** Number of $M1^{CT}$ neurons labeled in layer V from each thalamic region within the M1 portion of CFA; N=4 per group; error bars, SEM.

Extended Data Figure 6

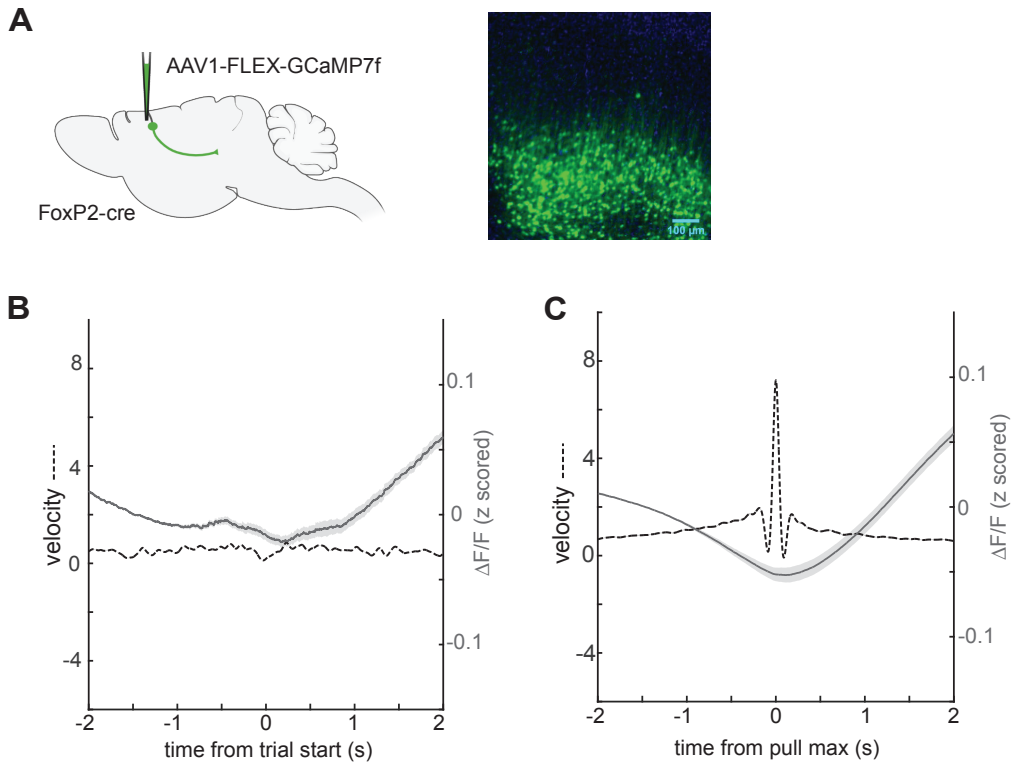

Extended Data Figure 6. Calcium imaging approach and $M1^{CT}$ activity

A Left, Schematic of workflow for calcium imaging of $M1^{CT}$ neurons; right, antibody amplified GCaMP7f signal, green; DAPI, blue. **B,C** Z-scored $\Delta F/F$ during unsuccessful trials **(B)** OR wheel pulls **(C)** mean, solid gray line; shaded area, SEM; Wheel velocity, dotted line; n=1078; N=4.

Extended Data Figure 7

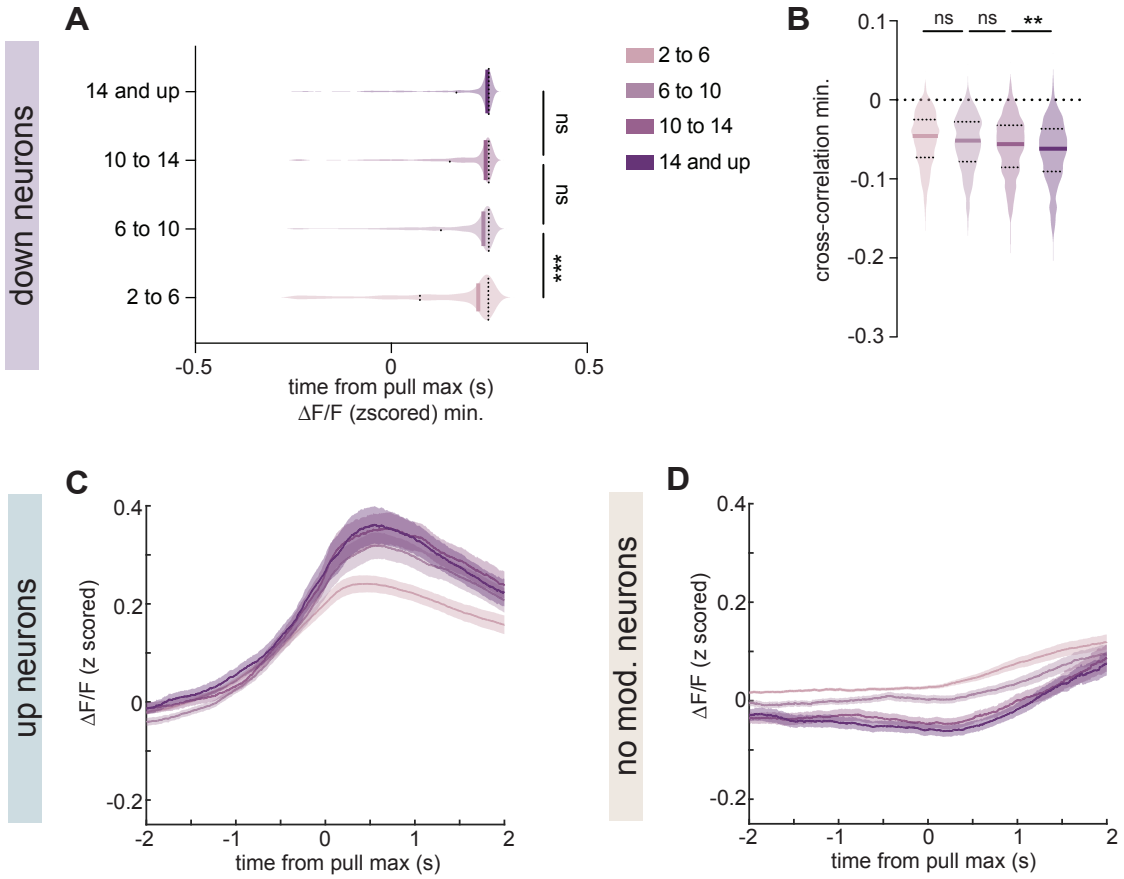

Extended Data Figure 7. Features of $M1^{CT}$ activity during pulls of varying velocity

As defined by ROC classification, units with decreases **(A,B)**, increases **(C)**, or no modulation **(D)** in activity during wheel pulls; legend for all as in **A**. **A,B** Distribution of time of ∆F/F minimum **(A)** or minimum of cross-correlation of wheel velocity to z-scored ∆F/F **(B)** during pulls of increasing velocity; thick, line, mean; thin lines, quartiles; One way ANOVA, multiple comparisons, $p<0.0001$, 2-6 v. 6 to 10; $p=0.1759$, 6-10 v. 10-14; $p=0.8196$, 10-14 v. 14 and up **(A)**. One way ANOVA, multiple comparisons, $p=0.0711$, 2-6 v. 6 to 10; $p=0.0657$, 6-10 v. 10-14; $p=0.0.039$, 10-14 v. 14 and up **(B)**. **C,D** Z-scored ∆F/F during pulls of increasing velocity; solid line, mean; shaded area, SEM.

Extended Data Figure 8

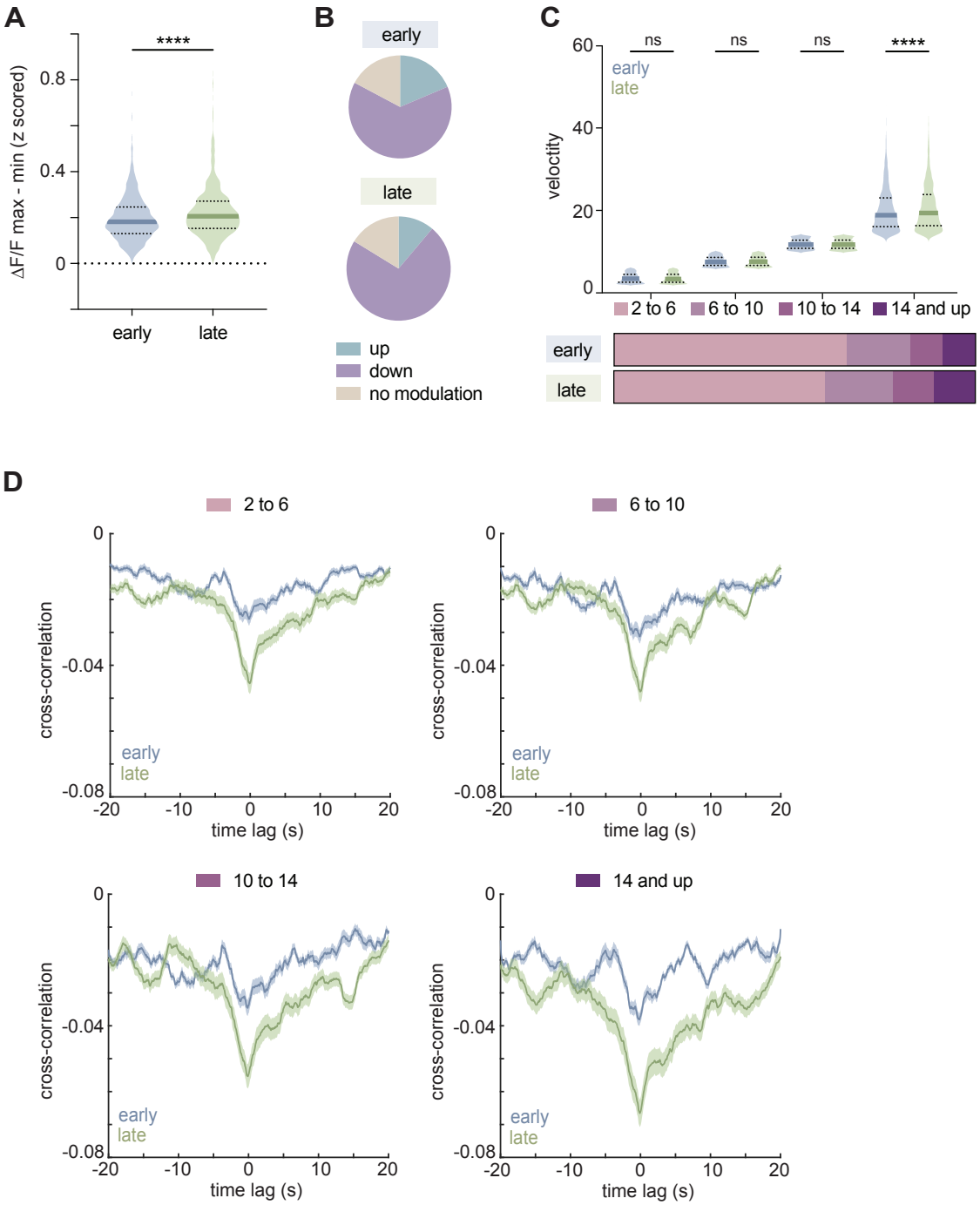

Extended Data Figure 8. Comparison of $M1^{CT}$ activity during early and late training

A Distribution of the difference in z-scored $\Delta F/F$ maximum and minimum before and during wheel pulls in down modulated neurons at early and late sessions; t-test, $p<0.0001$. **B** ROC based classification of all units over early and late sessions based on activity during wheel pulls. **C** Top, distribution of peak velocities in pulls of each velocity category in early (blue) or late (green) sessions; thick line, mean; thin lines, quartiles. One-way ANOVA, multiple comparisons, for early v. late, p=9890, 2-6; $p>0.9999$, 6-10 and 10-14; $p<0.0001$, 14 and up; Bottom, proportion of pulls in early or late sessions in each velocity category. **D** Cross-correlation of wheel pulls for early (blue) or late (green) training sessions of down modulated neurons to encoder velocity, grouped by increasing pull velocity; solid line, mean; shaded area, SEM.

Extended Data Figure 9

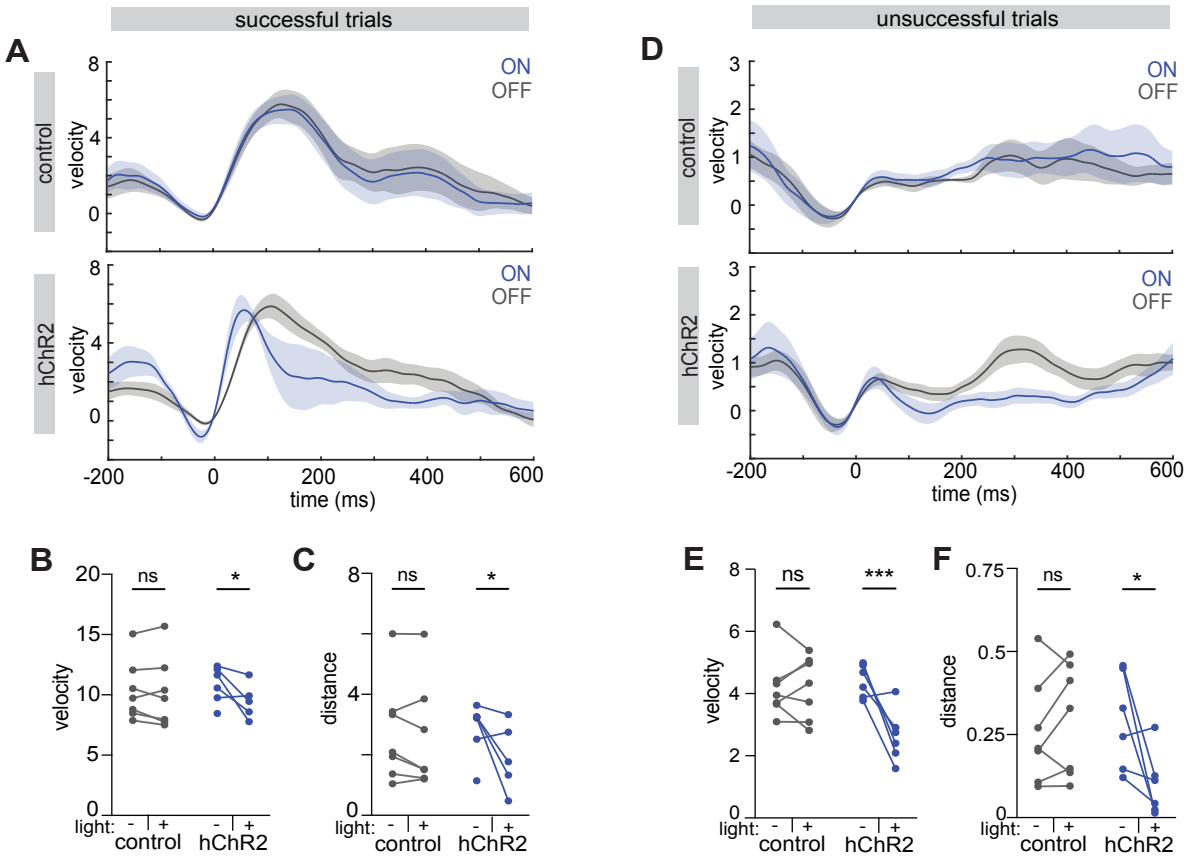

Extended Data Figure 9. Closed-loop optogenetic perturbation at trial initiation

A,D Velocity traces of successful **(A)** and unsuccessful **(D)** trials from control, top, and hChR2, bottom, animals during light, blue, and no light trials, gray, of closed-loop with light delivery at trial start; 0=trial start; blue bar denotes time of light; $p>0.9999$ (control), $p<0.0001$ (hChR2) **(A)**, $p>0.9999$ (control), $p<0.0001$ (hChR2) **(D)**, time x condition, two-way ANOVA; solid line, mean; shaded area, SEM. **B,E** Max velocity of successful trials **(B)** and unsuccessful trials **(E)** for each animal with light on or off in each group; two way ANOVA, multiple comparisons. **B**, $p=0.9741$ (control), $p=0.0204$ (hChR2)**; E**, $p=0.9997$, (control), $p=0.0073$ (hChR2); **C,F** Wheel distance traveled during successful **(C)** and unsuccessful **(F)** trials for each animal with light on or off for each group; error bars, SEM; **C,** Mixed-effect analysis, multiple comparisons, $p=0.8655$, (control), $p=0.0163$, hChR2**; F,** two way ANOVA, multiple comparisons; $p=0.7514$ (control), $p=0.0145$ (hChR2); N=7**,** control group; N=6, hChR2 group for **A-F.**

Extended Data Figure 10

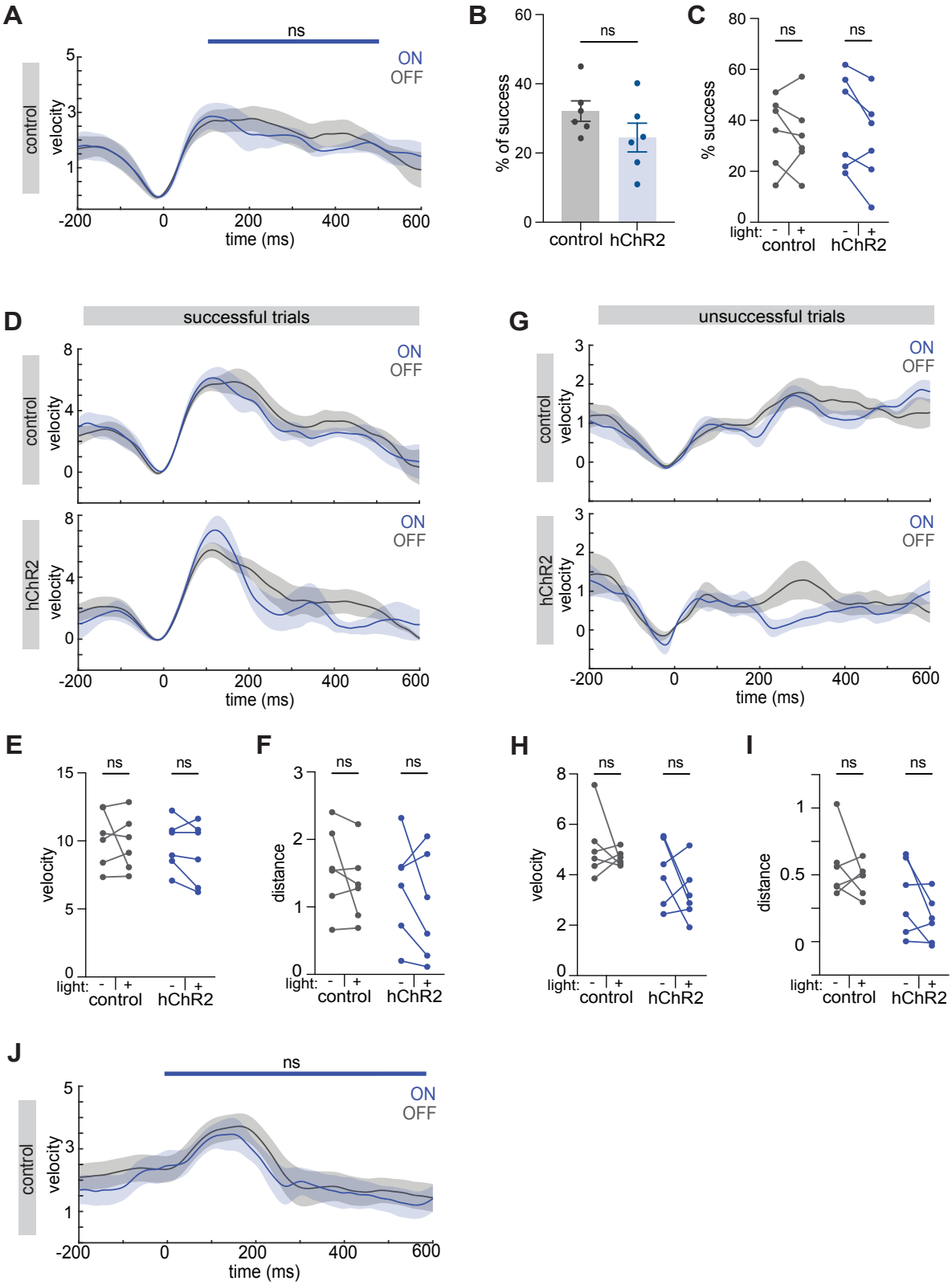

Extended Data Figure 10. Optogenetic manipulations of ongoing trials or prior to trial start

A Velocity traces of control animals during light, blue, and no light trials, gray, of closed-loop with light delivery at trial maximum; 0=trial start; blue bar denotes time of light; p=0.8618, time x condition, two way ANOVA solid line, mean; shaded area, SEM. **B** Percent of successful trials with light on; control, gray; hChR2, blue; error bars, SEM; two-tailed unpaired t-test, p=0.1644. **C** Percentage of trials that are successful for each animal with light on or off in each group; two-way ANOVA, multiple comparisons; p=0.8417, control; p=0.1467, hChR2**. D,G** Velocity traces of successful **(D)** and unsuccessful **(G)** trials from control, top, and hChR2, bottom, animals during light, blue, and no light trials, gray, of closed-loop light delivery to max of trial; 0=trial start; blue bar denotes time of light; p=0.4331 (control), p<0.0001 (hChR2) **(D)**, p>0.9999 (control), p<0.0001 (hChR2) **(G)**, time x condition, two-way ANOVA solid line, mean; shaded area, SEM. **E,H** Max velocity of successful trials **(E)** and unsuccessful trials **(H)** for each animal with light on or off in each group; two way ANOVA, multiple comparisons. **E**, p=0.9835 (control), p=0.7817 (hChR2)**; H**, p=0.5749 (control), p=0.9991 (hChR2); **F,I** Wheel distance traveled during successful **(F)** and unsuccessful **(I)** trials for each animal with light on or off for each group; error bars, SEM; two way ANOVA, multiple comparisons, **F,** p=0.5232, (control), p=0.3938, hChR2**; I,** p=0.5969 (control), p=0.2309 (hChR2); **J** Velocity traces of all pulls from control animals during light, blue, and no light trials, gray, of open loop light delivery with 100 ms light preceding trial start; 0=trial start; blue bar denotes time of light; p>0.9999, time x condition, two way ANOVA solid line, mean; shaded area, SEM; N=11, each group. **A-I**: N=6**,** control group; N=6, hChR2 group.